scientific reports

Check for updates

OPEN

Unraveling time-dependent roof stability dynamics in Iran's coal mines through laboratory-based rock displacement testing

Alireza Khoshmagham[1], Navid Hosseini[1✉], Reza Shirinabadi[1], Amir Hossein Bangian Tabrizi[1], Mehran Gholinejad[1] & Pooria Kianoush[1,2]

Roof stability is a critical concern in coal mines, as the potential for roof collapse poses a significant risk to miners' safety and productivity. Roof stability is heavily influenced by the time-dependent properties of the rock mass above the workings. This study uses rock displacement testing to examine the effect of time-dependent properties on roof stability and resistance reduction in coal mines in Iran. The study employed laboratory-based rock displacement tests on samples collected from coal mines in Iran, subjected to varying stress levels over time, to simulate the gradual deterioration of rock mass strength in underground mining conditions. The samples were monitored for displacement under these conditions to quantify the reduction in roof resistance over time and assess its effect on roof stability. The study found that areas with high stress at equilibrium gradually fail with time, and the stress transfers from the failure zone into deeper solid rock. The results demonstrate that varying viscous parameters can lead to different relaxation behaviors and stress distribution. Furthermore, incorporating strength degradation into numerical simulation can capture the failure under creep conditions and improve the accuracy of predicting time-dependent roof failure. This research aims to enhance safety measures and reduce the risk of collapses by investigating the time-dependent properties of roof stability through rock displacement testing in Iran's coal mines. The study's innovative approach uses numerical simulation based on the viscoelastic-plastic model to simulate the time-dependent behavior of the rock and incorporate strength degradation into the simulation. The results provide valuable insights into the time-dependent behavior of rock mass in coal mines in Iran and contribute to developing strategies for improving roof stability and lessening the chance of roof collapses. The instantaneous elastic strain was 4.35×10^{-4}, and creep simulation was activated to run for a time equivalent to 2×10^{6} s.

Keywords Roof stability, Coal mines, Time-dependent characteristics, Rock displacement testing, Viscoelastic plastic model, Strength degradation

Coal mining is a crucial industry that plays a significant role in the global economy. However, the safety of miners is always a concern due to the potential for roof collapses and other hazards[1–5]. In Iran, the impact of time-dependent properties on roof resistance reduction in coal mines is a critical concern that requires attention. It allows researchers to understand how the rock mass's strength changes under various stress levels over time. Coal mines are inherently dynamic systems, with roof stress varying significantly over time due to mining activities, geological changes, and environmental factors. Rock displacement testing is a widely used method to assess coal mine roofs' stability by measuring the pressure a roof can withstand over time[3,6–8]. This testing provides valuable information on the strength and stability of the roof and how it may deteriorate over time. Understanding the time-dependent characteristics of a roof is essential for ensuring the safety of miners and preventing accidents in coal mines[9–11].

[1]Department of Petroleum and Mining Engineering, South Tehran Branch, Islamic Azad University, 1777613651, Tehran, Islamic Republic of Iran. [2]National Iranian Oil Company, Exploration Directorate (NIOC-EXP), Tehran, Islamic Republic of Iran. ✉email: n_hosseini@azad.ac.ir; navid.hosseini@gmail.com

The country's three major coal mines, namely the Golestan, Kerman, and Zanjan provinces, have been evaluated for their roof stability and resistance. The results show that the Golestan coal mine, one of Iran's oldest and largest coal mines, has a relatively stable roof with a load-bearing capacity of 0.5–1.5 MPa. On the other hand, the Kerman coal mine has a more unstable roof with a load-bearing capacity of 0.2–0.5 MPa, which requires frequent roof support and monitoring. The Zanjan coal mine, known for its complex geology, has variable roof stability with a load-bearing capacity ranging from 0.1 to 1.5 MPa. Customized roof support systems are required to ensure stability and safety[4,12].

For example, on December 13, 2002, a roof collapse occurred at the Golestan coal mine in Iran, resulting in the deaths of 13 miners. The accident was caused by the failure of the roof due to the excessive stress generated by coal extraction. The mine's management had not properly monitored the roof's stability, leading to a catastrophic outcome[5]. Another example is the roof collapse at the Kerman coal mine in Iran on August 10, 2015, which resulted in the injuries of six miners. The collapse was caused by the sudden failure of the rock mass due to the weakening of the rock's strength over time[13–16]. These accidents highlight the importance of understanding the time-dependent characteristics of rock mass in coal mines and their impact on roof stability. Therefore, this study aims to investigate the impact of time-dependent properties and rock failure on roof stability, a crucial aspect of underground structure analysis[17–21].

Roof stability is a critical concern in coal mines, as roof collapse poses a significant risk to miner safety and productivity. In Iran, where coal mining is a significant industry, understanding the time-dependent characteristics of rock mass strength is essential for ensuring safe and efficient mining operations. Previous studies have investigated roof stability in coal mines, but most have focused on the immediate effects of rock failure without considering time-dependent properties. This study aims to fill this knowledge gap by investigating the impact of time-dependent properties on roof resistance reduction in Iranian coal mines through rock displacement testing[9,22,23].

Understanding the time-dependent behavior of rock mass strength is crucial for developing strategies to improve roof stability and reduce the risk of roof collapses[9,24–26]. This study will provide valuable insights into the factors contributing to roof stability and resistance reduction in coal mines, focusing on Iran's unique conditions. A new constitutive model is proposed that incorporates relevant features of rock mass behavior, including time-dependent behavior before and after failure, strain-softening behavior, and strength deterioration. Laboratory tests will determine the time-dependent behavior of rock in both pre-failure and post-failure regions, as well as its strength deterioration and strain-softening behavior.

Various factors can influence the roof failure process, and their impact should be investigated from a time-dependent perspective. Previous studies have identified directional horizontal stress and mine layout as significant factors affecting mine roof stability[6,27–29]. This study will investigate these factors and others to provide a more comprehensive understanding of roof stability.

Previous studies have shown that time-dependent characteristics, such as creep and relaxation, can influence the results of rock displacement testing; Peng[30] and others have demonstrated this effect[25,31–35]. In the past decade, the primary focus has been on stress redistribution around coal longwall mining panels, as examined by Kianoush et al.[16], who employed passive seismic velocity tomography and geostatistical estimation. Molinda and Mark[9] considered the rupture and cutting of the roof as a time-dependent process, noting that while roof rupture often damages the roof in the working area, roof collapse may occur months later[20,35–38].

In 2014, Gao et al.[39] simulated the shear failure of the roof at the entrance of an underground coal mine's main shaft using UDEC software. In 2017, Hosseini[5] also researched rockburst potential in longwall coal mining, utilizing passive seismic velocity tomography and image subtraction techniques[22]. Additionally, Hosseini and Khoei[40] presented a model for fluid flow in fractured porous media, focusing on interfacial conditions between the porous medium and fracture[22].

Recent studies have focused on developing numerical models incorporating time-dependent behavior and strength degradation[41]. For instance, Wang et al.[42] developed a viscoelastic-plastic model to simulate rock behavior under different stress conditions. Other studies have investigated the influence of factors such as directional horizontal stress and mine layout on roof stability[32,33,43]. Alejano and Alonso[25] examined the impact of creep and relaxation on roof stability, while Tran-Manh et al.[35] studied the effect of rock failure on roof stability.

Coal mine roof stability is crucial for underground mining, as roof collapse poses a significant risk to miners' safety and productivity. A key factor influencing roof stability is the time-dependent characteristics of the rock mass above the workings[42,44,45]. The rock mass is subject to forces like tectonic stress, gravity, and groundwater pressure, which can cause deformation and failure over time[17,24,46]. Rock displacement testing assesses roof stability by measuring how much a roof can withstand various pressures over time[16,40,47].

The time-dependent behavior of rock mass in coal mines is a complex phenomenon extensively studied in recent years. Several studies have investigated the impact of time-dependent properties on rock displacement testing, rock failure, and roof stability[42,44,45,48,49]. One key factor influencing roof stability is the time-dependent behavior of the rock mass above the workings[50–52]. Laboratory-based rock displacement tests have investigated the time-dependent characteristics of rock samples[53,54]. Researchers have also studied the time-dependent behavior of rock masses in coal mines, including creep and relaxation under different loading conditions[48,49].

For example, Weijian et al.[49] conducted an experimental study on rock mechanics under non-uniform loading conditions, finding significant creep behavior. Wu et al.[48] studied anchored jointed rock masses under uniaxial compression, observing significant relaxation behavior. Kasyap and Senetakis[52] and Li et al.[50] found that roof support significantly affects the deformation and failure of the rock mass.

Numerical simulations have also been used to study the time-dependent behavior of rock masses in coal mines[53–55]. For instance, Liu et al.[54] simulated the coal-rock parting-coal structure's slip and fracture instability mechanism and found significant time-dependent behavior. Long et al.[53] physically modeled paleo-uplift's influence on salt-bearing fold-and-thrust belt's structural deformation, observing significant deformation over time.

The study by Reeher et al.[41] highlights the importance of incorporating strength degradation into numerical simulations to predict failure under creep conditions.

Several recent studies have investigated various aspects of coal-rock interactions in deep coal mines. Xu et al.[22] reviewed coal-rock materials' damage dynamics and deformation. Ma et al.[56] explored the impact of coal thickness on the energy evolution characteristics of a roof-rock-coal-floor rock composite structure. Sun et al.[23] developed a jet grouting support strategy for controlling roadway deformation over time.

Yu et al.[57] proposed a new cutting roof technology for sustainable coal mine development, while Shang[38] and Shang et al.[58] investigated the failure mechanisms of surrounding rock in roadways subjected to repeated mining near coal seams. Zhang et al.[36] studied long-term deformation and bearing capacity under uniaxial compression, and Li et al.[4] examined the deformation and maintenance of deep-buried composite roof roadways.

Xie et al.[3] developed HPTL anchoring technology models for coal-rock composite roofs, while Dang et al.[10] researched the bearing characteristics of brackets in thick hard roof mining sites and the impact of blasting on roof control. Rong et al.[12] designed rockburst prevention systems based on the attenuation law of coal and rock vibration wave energy. Zhang et al.[2] studied the compaction and seepage characteristics of broken coal and rock masses in coal mining. Zhao et al.[1] investigated the failure properties of roadways with extra-thick coal seams and their control techniques.

However, previous literature reviews have overlooked the impact of time-dependent properties on rock displacement testing, particularly in Iranian coal mines. Moreover, most studies have focused on the immediate effects of rock failure without considering the time-dependent characteristics of rock mass strength. This study addresses this knowledge gap by investigating the impact of time-dependent properties on roof resistance reduction in Iranian coal mines through rock displacement testing.

As for the innovations of this study:

- We employ laboratory-based rock displacement tests, a novel approach in this field, to investigate the time-dependent characteristics of roof stability in Iranian coal mines.
- Our study uses a viscoelastic-plastic model to simulate rock's time-dependent behavior and incorporates strength degradation, a significant advancement in modeling rock behavior.
- Our research provides valuable insights into the time-dependent behavior of rock masses in Iran's coal mines. It contributes to developing strategies for improving roof stability and reducing roof collapse risk.

In conclusion, this study aims to investigate the impact of time-dependent properties and rock failure on roof stability in Iran's coal mines. The results will provide valuable insights into the time-dependent behavior of rock masses in Iranian coal mines and contribute to developing strategies for improving roof stability and reducing roof collapse risk.

Methodology

The objectives of this study are to address the following research questions:

1. How do time-dependent characteristics affect roof resistance reduction in coal mines in Iran?
2. Can a new constitutive model incorporate rock behavior, including time-dependent behavior, strain-softening, and strength deterioration?
3. What are the implications for improving roof stability and reducing roof collapses in coal mines?

To address these questions, we conducted laboratory-based rock displacement tests on Iran's coal mine samples subjected to varying stress levels over time to simulate gradual rock mass strength deterioration. We monitored sample displacement under these conditions to quantify roof resistance reduction and assess its effect on roof stability. The study found that areas with high equilibrium stress gradually fail with time, transferring stress to deeper solid rock. Results show that varying viscous parameters lead to different relaxation behaviors and stress distributions.

Our results demonstrate that incorporating strength degradation into numerical simulation can capture the failure under creep conditions and improve the accuracy of predicting time-dependent roof failure. Furthermore, we propose developing safety measures such as installing roof supports and monitoring systems to minimize the risk of roof collapses. These measures can be implemented in conjunction with the results of our study to enhance roof stability and ensure the safety of miners.

This study introduces the Burgers model as a critical tool for determining time-dependent parameters. Displacement tests, including creep and settling tests, were conducted on rock samples in the pre-failure area to validate this methodology. The Burgers equation's influence on laboratory test results was not considered. In the post-rupture area, indentation tests were performed. The expectation was that the deposition model, which incorporates visco-elastic behavior after fracture, could be used to determine time-dependent parameters of fractured rock[6,15,18,59]. However, the displacement-axial control model failed to achieve strain balancing. The flowchart of this study is shown in Fig. 1.

As illustrated Fig. 1, this study aims to investigate the impact of time-dependent characteristics on roof resistance reduction in Iranian coal mines. We will collect rock samples from coal mines and conduct laboratory-based rock displacement tests with varying stress levels to simulate the gradual deterioration of rock mass strength over time. The displacement of rock samples will be monitored, and the reduction in roof resistance will be quantified. The study will assess how this reduction affects roof stability in coal mines, analyze the results to understand the impact of time-dependent characteristics on roof resistance reduction and develop strategies to improve roof

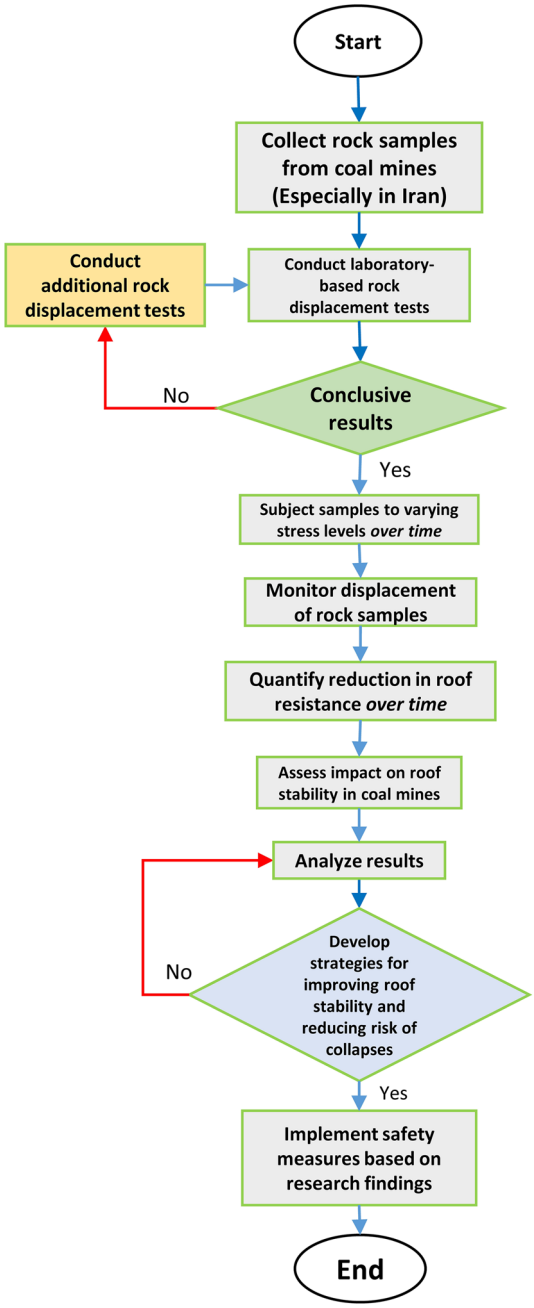

Figure 1. Flowchart of the study investigating the impact of time-dependent characteristics on roof resistance reduction in Iran's coal mines through rock displacement testing.

stability and mitigate the risk of roof collapses. Our findings will conclude and provide recommendations for the mining industry (Fig. 1).

Establishing a slacking model

The relationship between creep and slacking

Drescher and Handley[34], Zafar et al.[60], and Zafar et al.[61] distinguished creep and slacking as separate phenomena. Creep refers to the deformation of a material under constant stress over time, resulting from internal structural changes. Slacking, or relaxation, is the decrease in stress over time due to internal stress relaxation or reduced external forces[31,34,62,63]. Under unconfined conditions, creep is related to increasing stress and boundary forces, whereas slacking is associated with stress reduction and constant boundary deformation. As such, creep and slacking are two primary material behaviors from different boundary conditions. The material's inherent time-dependent properties must be continuous, regardless of whether it is subjected to creep or slacking tests.

After this step, we conducted numerical simulations of the unconfined relaxation test on a simulated rock sample using the Burgers material in the 3DEC 7.0 (Three Dimensional Distinct Element Code) software [https://docs.itascacg.com/3dec700/contents.html] (Described in Supplementary A)[39,46,64]. The experiment was designed to mimic real-world conditions, with a length ratio to the sample's radius maintained at a constant value of 2:1, a sample height of 10 m, and a radius of 5 cm. The model was primarily meshed in tetrahedral regions with an average edge length of 0.4 mm. The vertical velocity of the end of the model was set to zero, and a constant pressure was applied to the top of the model. After reaching equilibrium, the model remained fixed at a vertical distance above the sample (Fig. 2A). This setup allowed us to observe and analyze the creep and slacking behaviors of the Burgers material under controlled conditions, providing valuable insights for material testing and research.

Designing the 2:1 scale model enables researchers to capture the complexities of the rock mass's behavior at a smaller scale, which is impossible with larger scales. In particular, the model's 10 m height and 5 cm radius allow for studying the rock mass's behavior over a reasonable distance, which is crucial for understanding its long-term behavior.

The design was chosen to simulate conditions similar to those found in Iran's coal mines, which is the primary focus of the study. With a 2:1 scale, 10 m height, and 5 cm radius, researchers can simulate real-world conditions and study the rock mass's behavior under conditions similar to those in mining operations.

We activated the creep model during the six-hour investigation and monitored its stress using the 3DEC 7.0 program. The final insertion curve with parameters is specified in Fig. 2B. The simulation results are not just significant; they are crucial. They demonstrate that it can exhibit slacking behavior by manipulating its boundary conditions. It is evident in Fig. 2B, where the pressure in the sample gradually decreases over time, reflecting the initial pressure and constant boundary displacement. This simulation enables us to assess the effectiveness of the Burgers model's parameter settings in the context of the slacking curve, allowing for a thorough evaluation of their performance. If a similar slacking curve is observed in a laboratory slacking test, it becomes possible to determine the Burgers model parameters[15,56,65,66], thereby facilitating the practical application of our research findings.

The parameters used in our numerical simulation significantly impact its results. These parameters were chosen to mimic real-world conditions and accurately capture its behavior at a smaller scale. We divided it into small tetrahedral regions with an average edge length of 0.4 mm to ensure accuracy. The stress monitoring results (Fig. 2A,B) show that stress is monitored at a specific point within it where deformation occurs, but its exact location is not specified.

We used 3DEC 7.0 software to conduct our simulation and monitor its stress. We found that it exhibits slacking behavior when boundary conditions are manipulated. Our simulation results agree with theoretical calculations, validating our derived relaxation equation that generates creep and relaxation curves. The relaxation test provides a relationship between vertical stress and time, allowing for determining creep parameters from relaxation test data. This information is used to study time-dependent rock properties in the pre-failure region.

Relaxation model for coal mines

The Burgers model (described in Supplementary B) includes Kelvin and Maxwell units. Figure 3 shows the parameters m and k, representing the Kelvin and Maxwell units, respectively. Equations (1) and (2) illustrate the Burgers model for unconfined creep conditions, where k is the volume modulus. Equation (2) can be decomposed into its constituent parts. The right-hand side represents volumetric strain, while the other three terms describe deviatoric strain. As a result, the material exhibits elastic behavior under hydrostatic stress conditions and behaves like a rigid body under deviatoric stress conditions[67,68].

$$\varepsilon = \frac{\sigma}{9K} + \frac{\sigma}{3E_m} + \frac{\sigma}{3\eta_m}t + \frac{\sigma}{3E_k}\left[1 - \exp\left(\frac{-E_k t}{\eta_k}\right)\right] \tag{1}$$

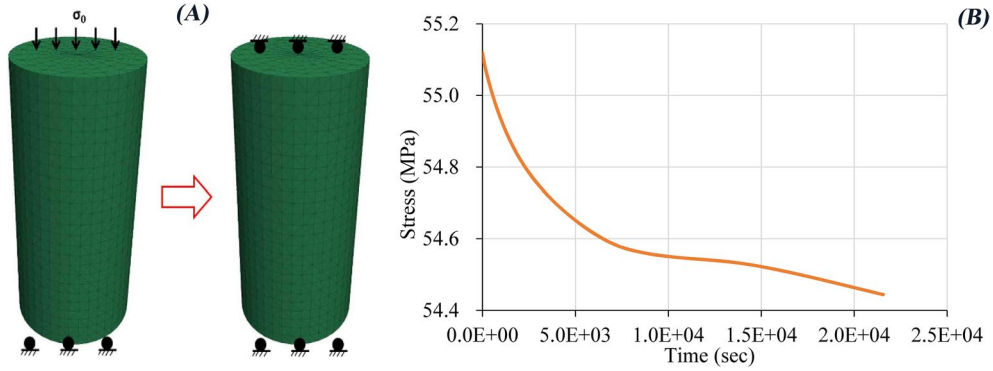

Figure 2. (**A**) Schematic of numerical simulation of the unlimited slacking (relaxing) experiment, (**B**) Slacking curve resulting from the numerical simulation[39].

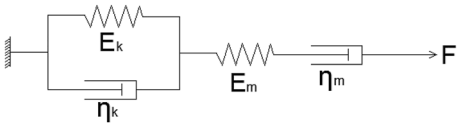

Figure 3. The Burgers model of relaxation, employing elastic modulus (E) and viscosity (η) in Maxwell (m) and Kelvin (k) units[67,68].

$$\varepsilon = \frac{1}{9K}\sigma + \left\{ \frac{1}{E_m} + \frac{1}{\eta_m}t + \frac{1}{E_k}\left[1 - \exp\left(\frac{-E_k t}{\eta_k}\right)\right]\right\}\frac{\sigma}{3} \tag{2}$$

The relationship between stress (σ) and strain (ε) at time t is described by the reciprocal of the bulk modulus ($\frac{1}{K}$) and the reciprocal of the apparent shear modulus $\left(\left\{ \frac{1}{E_m} + \frac{1}{\eta_m}t + \frac{1}{E_k}\left[1 - \exp\left(\frac{-E_k t}{\eta_k}\right)\right]\right\}\right)$. As time passes, the value of this term increases. The apparent shear modulus, which represents the resistance to deviatoric stress, gradually decreases with time. When the boundary displacement is fixed, the decrease in apparent shear modulus leads to the relaxation of stress within the rock. From this perspective, a creep model can theoretically explain the relaxation behavior observed in rock[15,23,34,67,68].

As mentioned earlier, using the Burgers model, the three-dimensional distinct element code (3DEC 7.0) is a commercial geotechnical software that simulates material behavior under various loading conditions. Based on viscoelasticity, which combines elasticity and viscosity concepts.

For Kelvin and Maxwell's units (Eqs. (3) to (4)):

$$\begin{aligned} F &= \dot{u}_k \times \eta_k + E_k \times u_k \\ \dot{F} &= \ddot{u}_k \times \eta_k + E_k \times \dot{u}_k \end{aligned} \tag{3}$$

$$\dot{u}_m = \frac{\dot{F}}{E_m} + \frac{F}{\eta_m} \tag{4}$$

In this context, the strain rate "$\dot{u}_k$" and strain "u_k" are represented by Kelvin units, while the strain rate "$\dot{u}_m$" and stress "F" are represented by Maxwell units.

The derivative of the stress "F" concerning time "t" can be obtained from Eq. (3). The notation for the various parameters can be found in Fig. 3. It is worth noting that "E_m" also represents the shear modulus.

The elastic portion of the Maxwell unit is exclusively active when the model is used to describe the time-independent or instantaneous response. Under this condition, the Burgers model exhibits elastic behavior described by E_m.

The total strain increment for relaxation is zero, represented by the Eq. (5).

$$\dot{u}_m + \dot{u}_k = 0 \tag{5}$$

This research aims to derive the relaxation equation and determine the creep parameters from relaxation test data.

The relaxation test provides a relationship between vertical stress and time. Therefore, it is necessary to express this relationship using a relaxation equation based on the derived model.

During unconfined testing, σ represents the axial stress. The deviatoric stress in the axial direction can be expressed as Eq. (6).

$$F = 2/3\sigma \tag{6}$$

Instead of the sum of Kelvin and Maxwell strain rates, as represented in Eq. (6), the total strain rate, including elastic volumetric strain rate, should be zero. The total strain rate can be expressed as Eq. (7):

$$\dot{u}_m + \dot{u}_k + \dot{u}_{vol} = 0 \tag{7}$$

where "$\dot{u}_{vol}$" represents the axial strain rate induced by volumetric strain, which is expressed as Eq. (8):

$$\dot{u}_{vol} = {}^{\sigma}/_{9K} \tag{8}$$

where K is the bulk modulus.

Following these equations, one can derive the relaxation equation under unconfined conditions as Eqs. (9) to (10).

$$\sigma = \sigma_0 \times \frac{\left[\left(r_1 + \frac{E_k}{\eta_k}\right)\exp(r_1 t) - \left(r_2 + \frac{E_k}{\eta_k}\right)\exp(r_2 t)\right]}{r_1 - r_2} \tag{9}$$

$$r1, r2 = \frac{1}{2\eta_k(1/E_m + 1/3K)}\left[-\left(1+\frac{\eta_k}{\eta_m}+\frac{E_k}{E_m}+\frac{E_k}{3K}\right) \pm \sqrt{\left(1+\frac{\eta_k}{\eta_m}+\frac{E_k}{E_m}+\frac{E_k}{3K}\right)^2 - 4\frac{E_k \times \eta_k}{\eta_m}\left(\frac{1}{E_m}+\frac{1}{3K}\right)}\right] \quad (10)$$

Figure 4A compares the relaxation relations obtained from numerical simulation and theoretical calculation, showing good agreement. It demonstrates the validity of the derived relaxation equation. The numerical simulation results in Fig. 4A are intended to represent a series of dots connected by lines rather than a continuous line. It is because the simulation was run using a discrete time-stepping algorithm, and the output is a sequence of system snapshots at regular time intervals. The viscoelastic-plastic model allows us to capture the time-dependent behavior of the rock mass, including creep and relaxation phenomena. The relaxation curve shows the gradual reduction in stress over time, a characteristic feature of rock deformation under constant load. By examining the creep and relaxation behavior of Burgers material using the same numerical simulation parameters, we can utilize Eqs. (1) and (9) to generate the creep curve and relaxation curve, respectively. A comparison of Fig. 4B,C reveals that both curves exhibit biphasic behavior, featuring a rapid stress drop in the initial stage and a gradual decline in the second stage. In contrast, relaxation tests exhibit a more rapid progression to the secondary stage due to continuous stress reduction. Interestingly, our results indicate that the duration of the first stage of the relaxation curve is comparable to that of the creep curve, with no noticeable differences. Therefore, it is recommended that the duration of a relaxation test in the pre-failure region be similar to that of a creep test.

Verification of the relaxation test for determining time-dependent parameters

This study's comprehensive investigation into rock's creep and relaxation behavior, validated by parameters determined from relaxation tests, has the potential to revolutionize the field. The combination of theoretical analysis and numerical simulation has verified the feasibility of relaxation tests for studying the time-dependent properties of rock in the pre-failure region. The simulation results confirm the possibility of determining parameters for the Burgers model using relaxation tests. To further validate this possibility, laboratory experiments involving various creep and relaxation tests on each specimen were conducted, and the resulting parameters were compared. If good agreement is achieved between the creep and relaxation test results, it could open up new avenues for using relaxation tests to study time-dependent rock properties, thereby enhancing our understanding and management of rock behavior[4,6,10,24,33,64].

In addition, this study attempted to extend the relaxation test method to the post-failure region by performing relaxation tests on specimens that had failed under uniaxial compression[7,18,20,69–71]. This approach can provide valuable insights into rock behavior after failure, assuming viscoelastic behavior for failed rock.

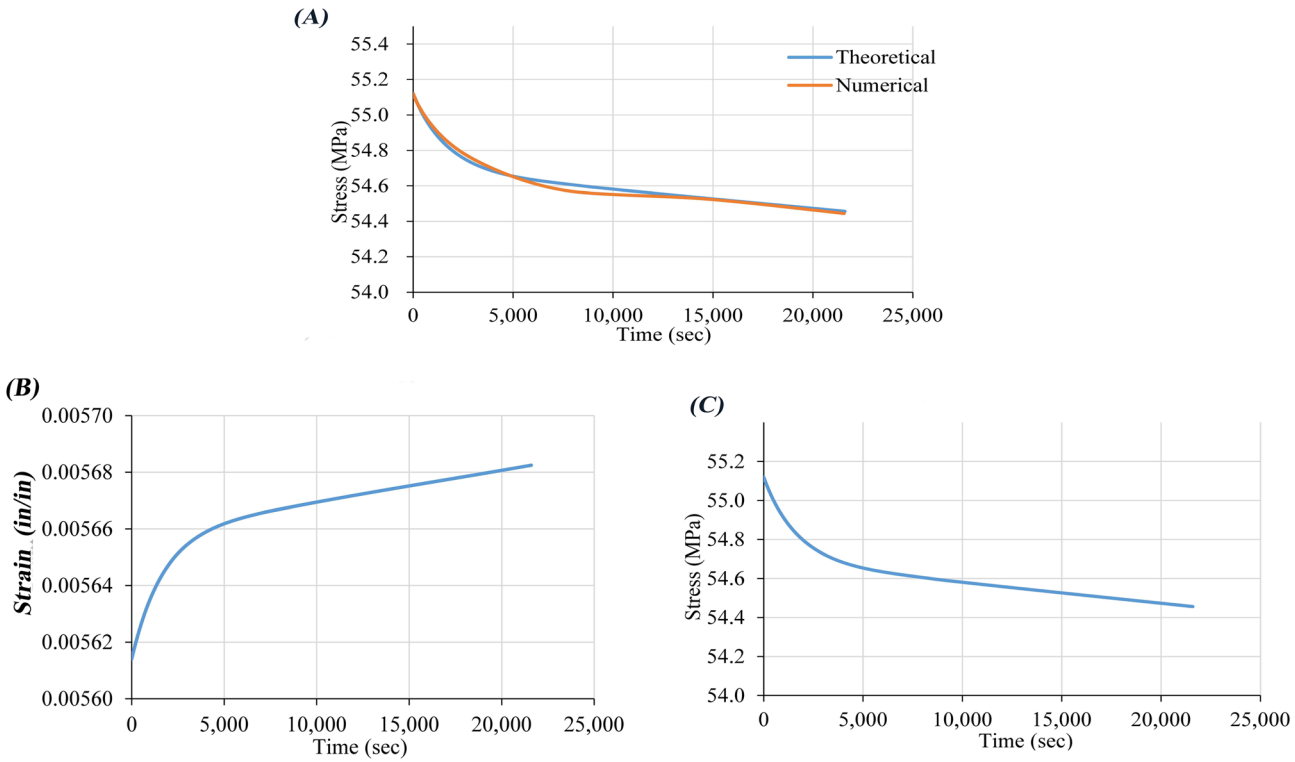

Figure 4. (**A**) Relaxation curve from numerical simulation, (**B**) creep curve, and (**C**) relaxation curve of theoretically calculated creep and relaxation curves with same parameters[34,60,61].

Time-dependent property variation and roof failure

Viscous parameter's curve fitting

A suitable fitting procedure is necessary to determine the viscous parameters from the relaxation test results. The expression of unconfined relaxation behavior, as depicted in Eq. (10), is complex and challenging to solve directly. Therefore, we proposed a novel fitting procedure to simplify this process. By representing the parameters r_1, r_2, and $\frac{E_k}{\eta_k}$ using three constants, a, b, and c, respectively, we can rewrite Eqs. (9) as (11). This Equation describes the relationship between stress ratio (σ/σ_0) and time (t) obtained from laboratory tests.

$$\frac{\sigma}{\sigma_0} = \frac{\left[(a+b)\exp(at) - (b+c)\exp(bt)\right]}{a-b} \tag{11}$$

Although expressions a, b, and c are intricate, they are constants in Eq. (11) and can be determined by curve fitting using the laboratory-determined stress-ratio-time relation. The unconfined compression test provides values of bulk and shear modulus, reducing the number of variables to three: E_k, η_k, and η_m. Three equations are available to determine these variables. We can obtain the values of the three unknown creep parameters by solving these equations.

To simplify the process, we can express the variables as a, b, and c. Once their values are determined through curve fitting, these constants can be substituted into the equations to obtain the three viscous parameters for the Burgers model.

$$\eta_k = \frac{-c}{(a+c)\times(b+c)\times\left(\frac{1}{E_m}+\frac{1}{3K}\right)} \tag{12}$$

$$E_k = c\eta_k \tag{13}$$

$$\eta_m = \frac{-1}{\frac{1}{\eta_k}\times(a+b+c)\times\left(\frac{1}{E_m}+\frac{1}{3K}\right)} \tag{14}$$

For the curve fitting process, we utilized the software Curve Expert 2.2 (2022) [https://www.curveexpert.net/]. This tool was instrumental in fitting the laboratory test data and determining the values of a, b, and c. The modified laboratory data, which established the relationship between time and stress ratio (σ/σ_0), was then used for the fitting process (Fig. 5). The software, guided by a user-defined model with the form of Eq. (11), determined the optimal values for the three variables, resulting in the best-fitting result (method is demonstrated in Supplementary Fig. C.1 to C.3). Finally, we substituted these three constants into Eqs. (12), (13) and (14) to obtain the three parameters for the Burgers model.

Variation in the time-dependent property of rock

Previous studies have neglected to explore the time-dependent properties of rock, resulting in a lack of understanding. In the early stages of deformation, researchers often rely on average creep values to characterize creep behavior. However, the underlying time-dependent mechanisms governing creep behavior in the later stages of failure remain unclear. Failed rock exhibits more relaxation than intact rock for the same duration, even when the relaxation test initiates from a lower stress level. This difference can be attributed to two possible explanations.

We propose a novel approach to address this issue that combines a viscoelastic framework with advanced modeling techniques. Our method incorporates a viscoelastic model to capture the time-dependent behavior of materials before and after failure while accounting for the nonlinear and irreversible nature of the material's response through a viscoplastic component. This integrated approach offers a fresh perspective and a

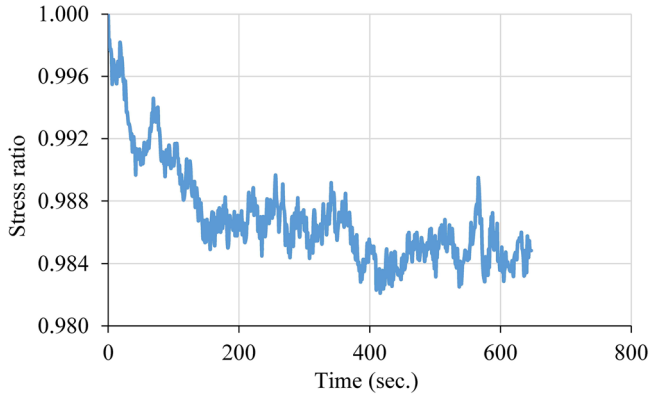

Figure 5. The relationship between time and F/F_0, as calculated from laboratory data. The relationship can be easily modified within Excel to visualize the correlation between these two variables[2,25].

more comprehensive understanding of the material's behavior, particularly in the post-failure region where time-dependent effects are crucial. The variation in viscous parameters demonstrates the variation in the time-dependent property.

The time-dependent property's variation before and after failure is still being determined. It may depend on plastic strain, suggesting constant time-dependent parameters before failure and varying parameters with plastic strain in the post-failure region. Alternatively, in the aftermath of failure, the temporal changes in the rock's properties may be minimal, with constant parameters serving as a proxy for the time-dependent behavior of failed rock material.

The parameters of the widely used Burgers model can be obtained from post-failure region relaxation curves. Curve Expert 2.2 software was used to perform curve fitting and determine the three constants (a, b, and c) in Eq. (11) . This model is known for accurately representing viscoelastic behavior and was instrumental in our research (Fig. 6A and Fig. 6B). Table 1 presents the parameters in the post-failure region, revealing that the

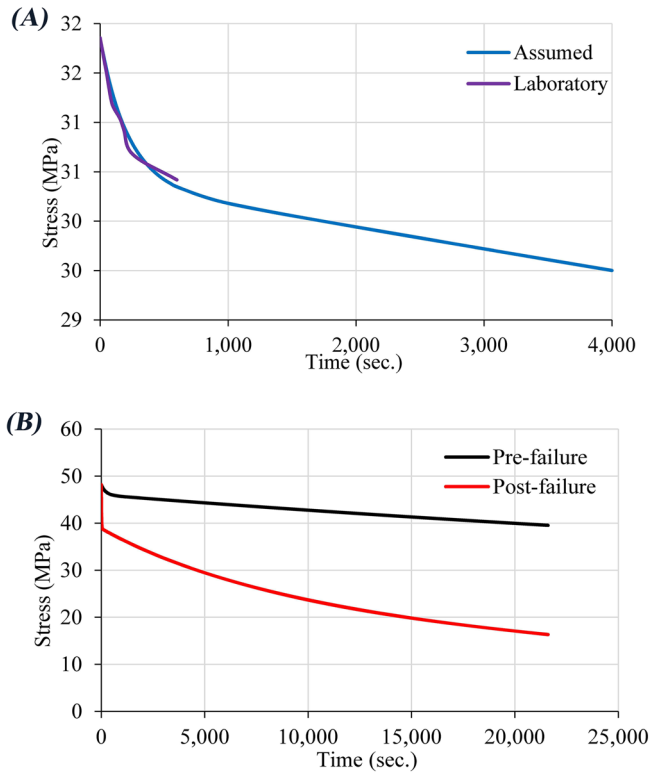

Figure 6. (**A**) Comparison of relaxation curves for assumed and laboratory models, (**B**) Comparison of relaxation curves, starting from the same stress values, before and after failure.

Parameter	Unit symbol	Value	Average
E_m	GPa	2.65×10^1	2.65×10^1
η_m	GPa × s	3.00×10^5	2.74×10^5
		3.98×10^5	
		2.40×10^5	
		1.56×10^5	
E_k	GPa	1.16×10^1	8.99×10^1
		8.41×10^1	
		9.03×10^1	
		6.96×10^1	
η_k	GPa × s	1.63×10^3	1.24×10^3
		1.09×10^3	
		1.29×10^3	
		9.37×10^2	

Table 1. Parameters in the post-failure region were determined based on previous studies[25,30,37,56].

difference between each creep parameter from the four relaxation tests is negligible. This finding underscores the robustness of our approach, suggesting that averaging each parameter over four relaxation tests allows for using averaged values for the viscous property of failed rock. These findings in the post-failure region further validate the effectiveness of our novel approach and are crucial for understanding the time-dependent behavior of rock materials.

Due to limited data, the parameters for the Burgers model in the pre-failure region are currently unavailable. However, our observations indicate that time-dependent parameters are more extensive in the pre-failure area than in the post-failure region. We incrementally increased those from the post-failure region to overcome this limitation and fit relaxation curves. This iterative process allowed us to approximate the parameters for the pre-failure region.

Figure 7A,B,C illustrate unconfined models and relaxation curves plotted with different viscous parameters for intact and failed rock, respectively. The curves for conditions with smaller viscous parameters initiate at the same stress level. The Fig. 7A shows that differences in viscous parameters result in significant differences in overall relaxation curve trends. Numerical simulations were executed on laboratory-scale rock specimens using determined parameters for intact and failed rock. Table 2 lists the parameters used in simulations.

Simulating time-dependent property variation

This study employed numerical simulations using the commercial geotechnical software three-dimensional distinct element code (3DEC 7.0) to investigate the influence of time-dependent property variation on rock behavior. The paper's numerical model construction and boundary stress application are founded on a specific engineering geological condition involving the behavior of rocks under various loading conditions, including creep, strain-softening, and strength degradation. The 3DEC 7.0 software employs the Burgers material to simulate unconfined relaxation tests on a virtual rock sample. Although designed for discontinuous media, 3DEC 7.0 can also simulate continuous media. This study pioneers using a finite-difference modeling approach to simulate the behavior of a rock mass under various conditions. The model, ingeniously divided into zones governed by a linear or nonlinear stress–strain relationship, offers a fresh perspective. The explicit solution scheme used in 3DEC 7.0 allows for the simulation of complex and nonlinear behaviors, adding a new dimension to our understanding of rock mass behavior.

The model was discretized into tetrahedral regions with an average edge length of 0.4 mm, resulting in approximately 100–500 zones and 1000–5000 nodes. This primary mesh size was the smallest unit for resolving local stress and strain fields within the rock mass. The model used a coarse mesh with an edge length of approximately 0.5 m for large-scale simulations. In contrast, a finer mesh with an average edge length of 0.4 mm was used for smaller-scale simulations.

The choice of mesh size involves a trade-off between accuracy and computational efficiency. A smaller mesh size would provide more accurate rock displacement simulations but at the cost of increased computational costs and resource requirements. The meshing process employed an adaptive technique, allowing larger zone sizes while maintaining the required accuracy. As a result, actual zone sizes can be up to approximately 0.5 m.

The 3DEC 7.0 model used in this study considers the boundary effect on results. Based on the distinct element method, it simulates complex rock behavior by breaking down rock masses into smaller elements interacting with each other. This model's boundary conditions mimic real-world scenarios, with the sample subjected to unconfined relaxation conditions. The rock sample is confined only at the top and bottom, while the sides are free to move, allowing it to relax and deform under its weight, mimicking coal mine conditions.

Parameter	Value
Time independent	
Density (Kg/m^3)	2562
Bulk modulus (GPa)	40.171
Shear modulus/M_{shear} (GPa)	26.461
Cohesion (MPa)	8.340
Friction angle (Deg.)	30.000
Tensile strength (MPa)	6.891
Time dependent	
Pre failure	
$M_{viscosity}$ (GPa × s)	2.74×10^6
K_{shear} (GPa)	4.51×10^2
$K_{viscosity}$ (GPa × s)	9.92×10^4
Post failure	
$M_{viscosity}$ (GPa × s)	2.74×10^5
K_{shear} (GPa)	9.03×10^1
$K_{viscosity}$ (GPa × s)	1.24×10^3

Table 2. Employed parameters in time-dependent simulation.

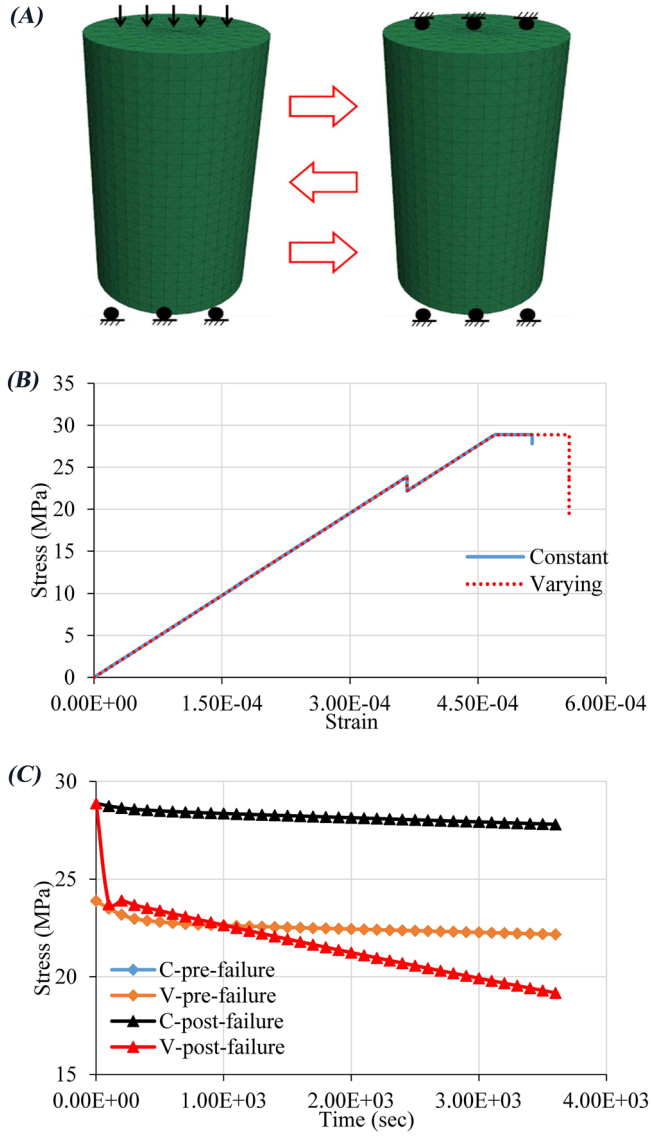

Figure 7. (**A**) Model for unconfined compression test with relaxation tests, (**B**) Stress–strain curve for unconfined compression tests with relaxation test, Relaxation curves for the four relaxation tests.

A viscoelastic-plastic model simulates time-dependent rock behavior, capturing complex interactions between the rock and its environment, including creep and relaxation effects. Validated using laboratory test results, it accurately predicts rock behavior under various loading conditions.

A study simulated two unconfined compression tests, each with a relaxation test in pre- and post-failure regions. The bottom of the model was fixed, and a velocity boundary was applied from the top. Initially, the simulation applied a velocity boundary, followed by a fixed top boundary to simulate relaxation for one hour. Then, the simulation changed to a velocity boundary to apply a load in the post-failure range. Stress, strain, and creep time were monitored diligently to ensure the accuracy and reliability of the results.

The two relaxation tests in the pre-failure and post-failure regions were initiated at the same stress level. The difference between these tests lies in the time-dependent parameters: one specimen was assigned constant parameters, while the other varied with time-dependent parameters. Figure 7B,C present the resulting stress–strain and relaxation curves.

The study's results are significant, revealing that the behaviors of the two models are identical in the pre-failure region but differ in the post-failure region. The stress–strain and relaxation curves are similar in the pre-failure region, indicating that time-independent and time-dependent behaviors are similar before failure. However, different behaviors occur when changing time-dependent parameters in the post-failure region. The specimen with varying viscous parameters relaxed more stress than constant parameters for the same duration in the post-failure region, indicating that relaxation behavior is more significant. These results represent an essential step forward in understanding rock mass behavior (Fig. 8).

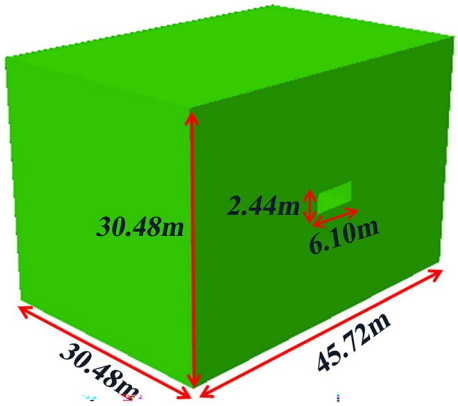

Figure 8. Model dimension of time-dependent characteristics.

The study also investigated the influence of time-dependent property variation on excavation with a rectangular cross-section in a homogeneous massive rock mass of marble. Simulations demonstrate the influence of time-dependent property variation on stress distribution and plastic zone formation between two different simulation methods.

Simulations considered size effects for rock mass stability, assuming that in-situ stress and mining layout was responsible for failure around underground excavation at equilibrium. As a result, excavation in an assumed in-situ stress field could introduce plastic zones in the surrounding rock mass. In creep simulations, one model changed parameters for failed zones while the other did not. The simulations assumed an angle of 60° between the longitudinal axis and maximum horizontal stress.

Limitation and advantages

Limitations

1. Sample size: The number of rock samples collected from coal mines in Iran may be limited, which could influence the generalizability of the outcomes.
2. External factors: External factors, such as environmental conditions or geological features, could impact the results of the rock displacement testing.
3. Time constraints: Conducting laboratory-based tests to simulate the gradual deterioration of rock mass strength over time may be time-consuming and potentially delay the research process.
4. Cost: The cost of conducting rock displacement testing in a laboratory setting can be significant, which may limit the scope of the research[3,14,17].

Advantages

1. Improved safety: By understanding the time-dependent characteristics of roof resistance reduction in coal mines, researchers can develop strategies to enhance safety measures and prevent roof collapses.
2. Enhanced productivity: By improving roof stability in coal mines, the overall productivity of the mine can increase as the risk of downtime due to roof collapses is minimized.
3. Global impact: The potential global impact of the findings of this study is substantial. It could contribute to better risk management practices and safety standards in underground mining operations worldwide, thereby benefiting the entire industry.
4. Strategic planning: The practical implications of this research are significant. The insights gained from this investigation can help mining companies in Iran and other regions develop long-term strategies for maintaining roof stability and ensuring the sustainability of coal mining operations[15,35,37,60,61,68,72,73].

In conclusion, the study on the impact of time-dependent characteristics on roof resistance reduction in Iranian coal mines through rock displacement testing is important in the mining industry. It underscores the critical need to understand factors affecting the roof stability of underground mining operations. This research can potentially enhance safety measures and risk management practices globally in coal mines. However, it is crucial to acknowledge its limitations. Rock displacement testing results may not fully replicate real-world conditions, and additional factors such as geological conditions, mining methods, and support systems can also influence roof stability. Nevertheless, this study proposes practical insights that can guide strategies for improving safety and productivity in coal mining, thereby contributing to a safer working environment for miners and the industry's sustainability.

Results

The results of this study are crucial for improving safety measures and risk management practices in coal mines in Iran. By understanding the impact of time-dependent characteristics on roof resistance reduction, mining companies can implement better strategies to prevent roof collapses and ensure the safety of their workers. Additionally, the findings of this research could have broader implications for underground mining operations globally, as the insights gained from this study can inform best practices for enhancing roof stability and reducing the risk of accidents in coal mines. Overall, this research contributes to the advancement of the mining industry by addressing a critical safety concern and providing valuable information for improving safety standards in coal mines.

Relaxation laboratory test

This study investigated the behavior of sandstone specimens from coal mines under relaxation tests. The specimens were prepared and tested using a servo-controlled compression testing system to simulate unconfined compression conditions. The testing methodology involved applying an initial load and strain control to simulate failure. The test procedure involved preparing sandstone specimens with a diameter of 50.8 mm (2 in.) and testing them under unconfined compression conditions. Two testing phases were conducted: (1) applying an initial load with axial displacement control, followed by strain control to simulate failure, and (2) relaxing the specimen after failure and monitoring its stress–strain behavior.

The results showed that the sandstone specimens exhibited shear failure with a major failure plane. The rock strength varied significantly, ranging from 53.06 to 61.85 MPa, with an average strength of 58.12 MPa. Failure conditions were categorized as non-persistent or persistent. Table 3 summarizes the test results, including strength, lateral deformation at failure, and failure condition. Figure 9A,B illustrate the shear failure mode, while Fig. 9C,D,E,F show photographs of the specimens before and after testing.

The stress–strain curves for the unconfined compression tests exhibited several notable features. Figure 10A,B show typical stress–strain curves and stress-lateral deformation curves, respectively. The stress–strain curves did not reach the residual stage, and tests were terminated when the maximum range of the circumferential strain gauge was reached.

We conduct unconfined compression tests with relaxation testing (Fig. 10C), which involves applying an initial load with a displacement magnitude of 0.76 mm using axial displacement control, followed by controlled

Test No	Strength (MPa)	Average strength (MPa)	Lateral deformation at failure (mm)
1	53.061	58.120	0.2770
2	56.92		0.4270
3	61.851		0.3530
4	60.661		0.2770
Test no	**Failure condition**	**Lateral deformation starting relaxation (mm)**	
5	Non-persistent failure	0.762	
6	Persistent failure	0.762	
7	Non-persistent failure	0.762	
8	Non-persistent failure	1.270	
9	Persistent failure	1.270	
10	Persistent failure	1.270	

Table 3. Unconfined compression test and failure condition result summary.

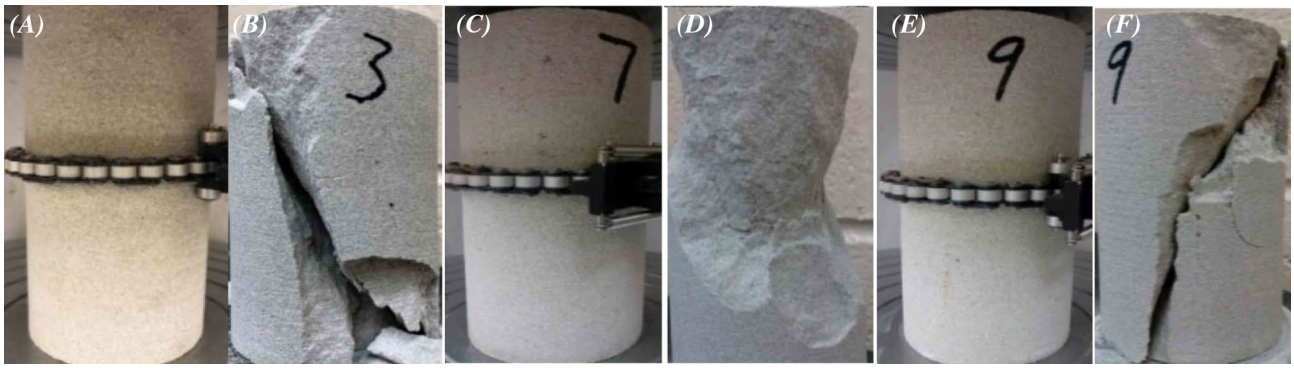

Figure 9. Sandstone specimen failure patterns, (**A**) Before testing, (**B**) After testing, (**C**) Before testing (Non-persistent major failure plane), (**D**) After testing (Non-persistent major failure plane), (**E**) Before testing (Persistent major failure plane), **F**) After testing (Persistent major failure plane).

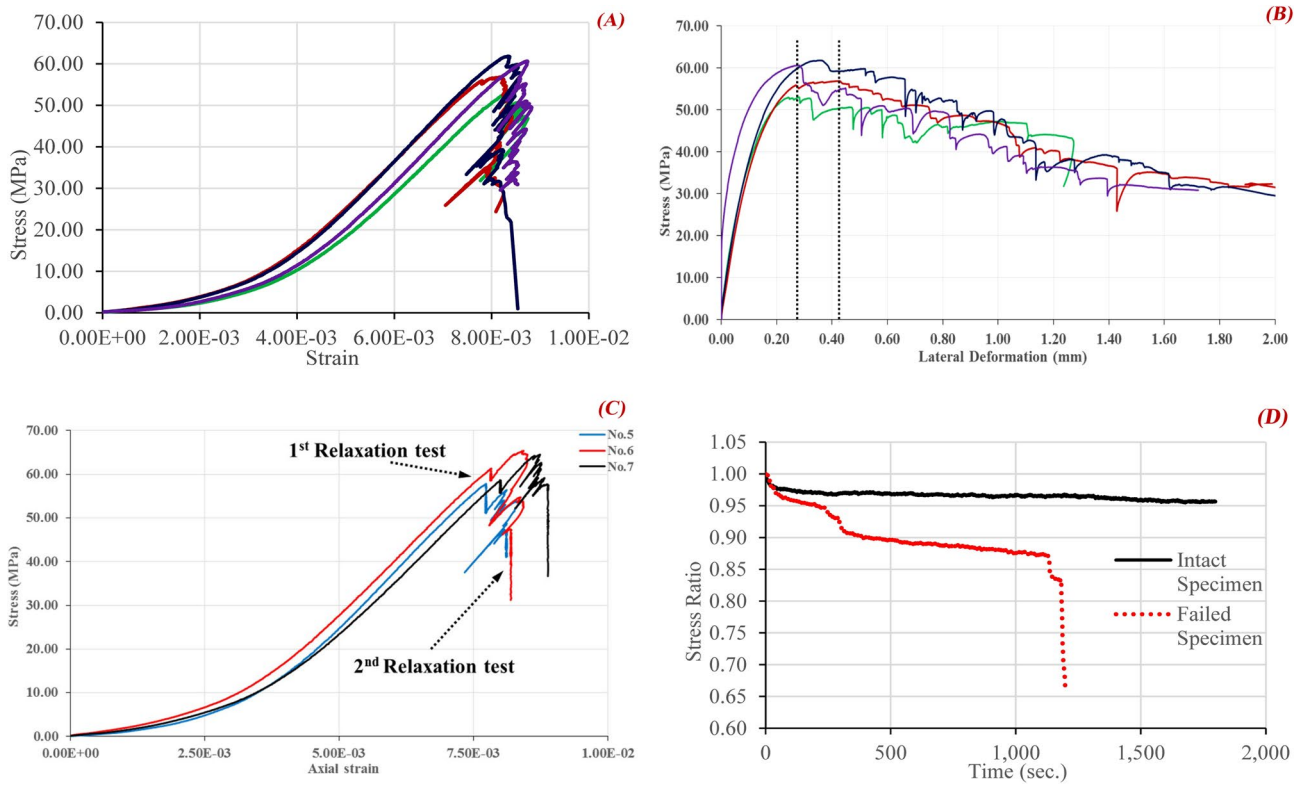

Figure 10. Unconfined compression tests, (**A**) Stress-axial strain curve, (**B**) Stress-lateral deformation curve, (**C**) Stress–strain curves for tests No. 5, No. 6, and No. 7, (**D**) Relationship between time and stress ratio during relaxation tests in pre-failure and post-failure regions.

circumferential strain to induce failure in the specimens. Figure 10D illustrates the relationship between time and stress ratio during relaxation tests in pre- and post-failure regions. Over 30 min, the stress relaxes more from failed than intact specimens.

In conclusion, this investigation underscores the importance of understanding relaxation behaviors in sandstone specimens from coal mines. The results show that relaxation behaviors depend on the stress condition initiating the test, with failed specimens relaxing more than intact ones. The study reveals distinct patterns in pre-failure and post-failure regions. Two phenomena contribute to stepwise relaxation behavior in the post-failure region: the propagation of non-persistent failure planes during stress relaxation and the shear-off of asperities along the major failure plane.

Laboratory experiment design

Three rocks of varying sizes of coal, including sand shale, limestone, and lime shale, were obtained from different southern, central, and northern Iran regions. Fifty-millimeter (two inches) core samples were prepared according to the recommended ASTM standard and tested in a material testing system (MTS) machine (presented in Supplementary D). The characteristics of the tested rocks are presented in Table 4. The laboratory tests were conducted in two groups: creep and relaxation tests at various stress and strain levels for each sample.

Rock type	Density (Kg/m^3)	Young modulus (GPa)	UCS (MPa)
Limy shale	2621	4.09	23.49
		3.67	22.04
		9.56	89.40
Sandy shale	2625	12.14	101.62
		22.27	161.22
		14.04	104.95
Shaly limestone	2659	17.22	82.50
		22.35	141.03
		19.15	89.38

Table 4. Rock mechanical properties of tested samples.

This study investigated rock displacement testing on coal mine samples from Iran, subjected to varying stress levels over time, to simulate the gradual degradation of rock strength. The value of rock strength deterioration is determined as a function of cumulative effective viscous strain using the Burgers model. This viscoelastic-plastic model incorporates both creep and relaxation behaviors. The model was calibrated through laboratory-based rock displacement tests, which simulated the gradual deterioration of rock mass strength over time by applying varying stress levels. Varying viscosity parameters led to distinct relaxation behaviors, which were accompanied by different stress distributions. These variations highlight the importance of considering cumulative effective viscous strain in understanding rock strength deterioration.

As shown in Table 4, the third Limy shale sample, distinct from the others, may have a unique microstructure or mineral composition affecting its mechanical properties. It could influence its response to stress and deformation over time, leading to differences in creep and relaxation behavior compared to the other samples.

To understand this sample's distinct behavior, it is essential to investigate its characteristics further. It may involve additional laboratory tests, such as scanning electron microscopy (SEM), X-ray fluorescence (XRF), or energy-dispersive spectroscopy (EDS), to analyze the mineral composition and microstructure. Numerical simulations using various constitutive models can also evaluate how the sample's unique properties affect its mechanical behavior under different stress conditions. This information will improve the accuracy of the study's conclusions and provide a comprehensive understanding of the time-dependent characteristics of roof resistance reduction in Iran's coal mines.

First group

The primary purpose of the first group of tests was to validate the method of relaxation testing by comparing the parameters obtained from creep tests and relaxation tests in the pre-rupture region. To confirm this method, it is necessary to compare the results between the two test methods. Since conducting a creep test on a ruptured sample is challenging, it is impossible to compare results in the post-rupture region. Therefore, this experiment focused on comparing results in the pre-rupture region. The experiment aimed to perform three creep tests and two relaxation tests on two samples with different pressure levels of 70%, 75%, 80%, 85%, and 90%. The parameters determined from the two relaxation and three creep tests were averaged and compared for each sample (Fig. 11). For all samples in Group 1, the parameters differed based on test methods to eliminate variables in the results by homogenizing samples. This group includes tests performed on three shaly-limestone samples.

The second group

The second group of tests aimed to accomplish two objectives. Creep tests were performed on samples at two unconfined compression stress levels. In contrast, relaxation tests were conducted at different strain levels of the unconfined compression test on three samples of the same rock type. The first three relaxation tests were designed to occur in the pre-failure region and were compared with creep test results. The primary goal of this group was to investigate the time-dependent behavior of the rock.

The second objective was to examine the time-dependent characteristics of fractured rock. Previous relaxation tests on fractured rock have shown significant relaxation in the post-failure region, indicating that fractured rock can transfer more pressure to surrounding rocks than intact rock. The last two relaxation tests were conducted in the post-failure region to study the behavior of failed samples. By comparing relaxation curves from both regions, we can determine the differences in relaxation behavior between intact, failed, and fractured rock.

Suppose the time-dependent behavior in the post-failure region appears viscoelastic. In that case, different parameters can be used to determine the model parameters for fractured rock, as in the pre-failure region. Conversely, parameter differences before and after discontinuities can indicate variations in time-dependent properties.

In summary, the second group included samples tested by creep test in the pre-failure zone and others subjected to relaxation tests in both pre-failure and post-failure zones. The combination of creep and relaxation tests in the pre-failure area confirms the effectiveness of relaxation testing in analyzing time-dependent characteristics of intact, failed, and fractured rock.

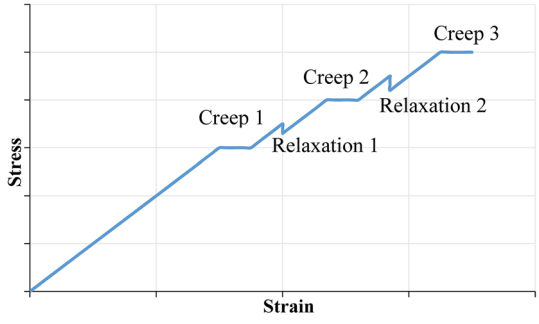

Figure 11. Schematic of the laboratory test procedure for each specimen, which shows the parameters determined from two relaxation tests and three creep tests.

Laboratory results

The relaxation tests can be used to determine the viscous parameters of rock based on the proposed procedure in this chapter. Figure 12A,B show examples of creep curves and relaxation curves from laboratory tests and their fitted models. The excellent agreement between the laboratory results and fitted models demonstrates that the Burgers model can accurately represent the time-dependent behavior of rock.

The stress–strain curves in Figs. 5 and 12 exhibit fluctuations due to two primary factors: the rock sample's viscoelastic properties and potential noise in the data acquisition process. The rock samples' viscoelastic behavior is characterized by a combination of elastic and viscous responses, leading to sudden changes in strain and stress. Additionally, the rock samples experienced creep behavior, where the material deforms under constant stress over time. This creep behavior can lead to fluctuations in the measured strain and stress values.

Potential noise in the data acquisition process may have contributed to the observed fluctuations, as small measurement or instrument calibration errors can amplify over time. However, the tests were conducted using a controlled laboratory setup, where the stress levels were applied step-wise, simulating the gradual increase in stress due to mining activities and geological changes.

Incorporating strength degradation into numerical simulation can capture the failure under creep conditions and improve the accuracy of predicting time-dependent roof failure. The viscoelastic-plastic model used in this study accounts for the time-dependent behavior of the rock mass, including creep and relaxation, allowing for a more realistic representation of the rock's mechanical behavior. Overall, the fluctuations observed in Figs. 5 and 12 are attributed to the complex interactions between the rock sample's mechanical properties, testing conditions, and experimental setup.

The Burgers model's viscous parameters were determined using creep and relaxation tests on three shaly limestone specimens in Group 1. The results were compared to assess the effectiveness of relaxation tests in obtaining viscous parameters. Table 5 presents the averaged parameters from each creep test and relaxation test, showing a slight variation in the averaged parameters between the two types of tests. However, further averaging the parameters over the three specimens reduces this variation.

The test results for Group 2 did not conform to the original design due to heterogeneity in the specimens. The tests were separated into pre-failure and post-failure parts, with each part analyzed separately. Figure 13A through, Fig. 13B,C, show the fitted Burgers model parameters for each test, with data points representing parameters from one creep test or relaxation test. The data points from creep tests and relaxation tests on the same rock type have similar shapes but differ in color.

The distribution of the data points demonstrates that some parameters determined from different test methods show good agreement, such as the value of η_m for sandy shale and limy shale. Others show significant differences,

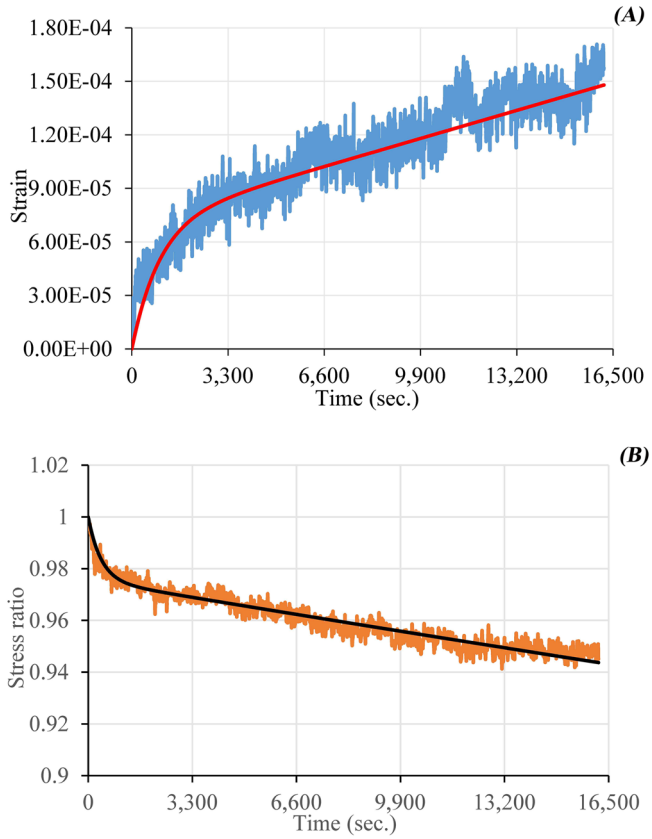

Figure 12. Curve fitting result of Burgers model for (**A**) creep test, and (**B**) relaxation test.

Specimen (Sample)	Stage	K (psi)	E_m (psi)	η_m (psi*s)		E_k (psi)		η_k (psi*s)	
		Value	Value	Value	Average	Value	Average	Value	Average
1	Relaxation 1	2.15×10^{06}	1.42×10^{06}	4.87×10^{11}	1.04×10^{12}	5.46×10^{07}	7.57×10^{07}	6.36×10^{10}	7.44×10^{10}
	Relaxation 2			1.60×10^{12}		9.67×10^{07}		8.52×10^{10}	
	Creep 2			9.75×10^{11}	1.17×10^{12}	4.80×10^{07}	5.16×10^{07}	4.53×10^{10}	4.56×10^{10}
	Creep 3			1.37×10^{12}		5.51×10^{07}		4.59×10^{10}	
2	Relaxation 1	1.79×10^{06}	1.18×10^{06}	4.87×10^{11}	8.59×10^{11}	8.96×10^{07}	7.48×10^{07}	7.23×10^{10}	5.88×10^{10}
	Relaxation 2			1.23×10^{12}		6.00×10^{07}		4.52×10^{10}	
	Creep 2			5.95×10^{11}	7.53×10^{11}	4.53×10^{07}	4.40×10^{07}	3.79×10^{10}	3.60×10^{10}
	Creep 3			9.11×10^{11}		4.26×10^{07}		3.41×10^{10}	
3	Relaxation 1	1.86×10^{06}	1.23×10^{06}	6.12×10^{11}	9.01×10^{11}	4.77×10^{07}	4.49×10^{07}	1.69×10^{10}	1.72×10^{10}
	Relaxation 2			1.19×10^{12}		4.21×10^{07}		1.74×10^{10}	
	Creep 2			6.89×10^{11}	8.00×10^{11}	5.73×10^{07}	7.30×10^{07}	1.96×10^{10}	3.69×10^{10}
	Creep 3			9.10×10^{11}		8.87×10^{07}		5.41×10^{10}	
Average	Relaxation	1.93×10^{6}	1.28×10^{6}		9.34×10^{11}		6.51×10^{07}		5.01×10^{10}
	Creep				9.08×10^{11}		5.62×10^{07}		3.95×10^{10}

Table 5. Comparison of creep parameters from creep and relaxation tests from first group of tests.

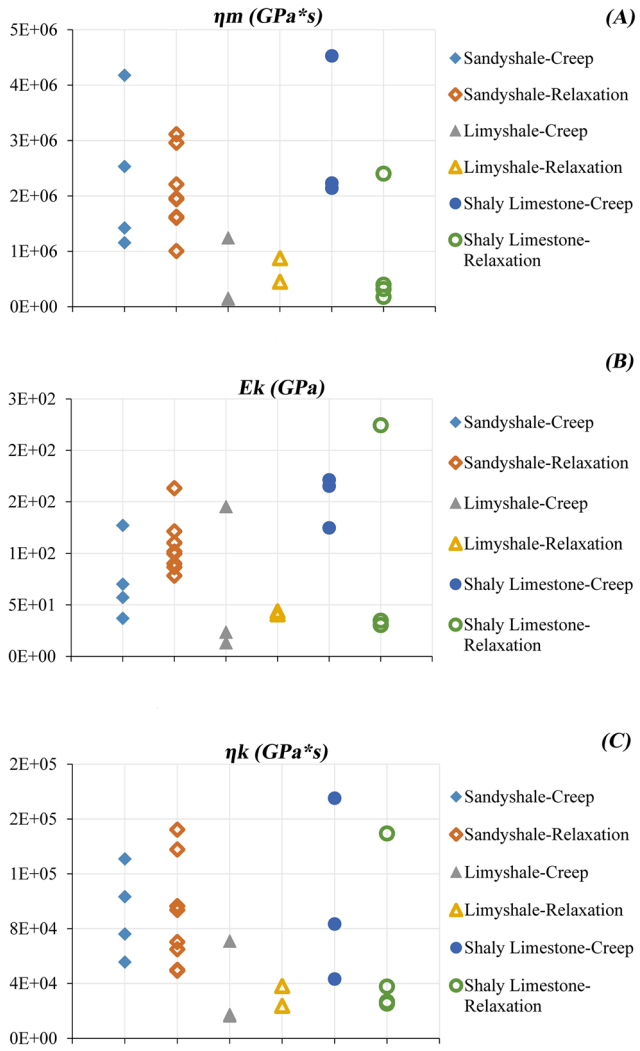

Figure 13. Values of (**A**) ηm (GPa*s), (**B**) E_k (GPa), (**C**) ηk (GPa*s) for different rocks with creep and relaxation tests from second group of tests for different rocks with creep and relaxation tests from second group of tests.

such as the value of E_k for all rocks. These differences can be confirmed by quantifying the distribution of these parameters with mean and standard deviation in Table 6. This study comprehensively overviews our experimental setup, sample selection, and data analysis procedures. We compare our results to theoretical models and simulations, confirming their reliable findings. The test results in Fig. 13 show significant dispersion, a common issue in laboratory-based rock displacement testing. This dispersion arises from instrument errors, sample heterogeneity, and experimental setup limitations. In this case, the rock samples' complexity likely contributed to the high dispersion observed.

To improve accuracy, we employed a viscoelastic-plastic model to simulate the time-dependent behavior of the rock mass, accounting for creep and relaxation phenomena. Incorporating strength degradation into numerical simulation enables accurate predictions of creep-induced failure and roof stability. Our innovative approach using numerical simulation with the viscoelastic-plastic model can mitigate dispersion and provide more accurate predictions of roof stability. To further validate our findings, we recommend conducting additional tests with improved testing conditions and sample preparation to reduce dispersion. We also plan to explore statistical analysis and data reduction techniques to quantify uncertainty in test results (Fig. 13).

The study designed some relaxation tests to conduct in the post-failure region to investigate the time-dependent property of failed rock. The results of these tests can determine the parameters for the Burgers model. However, the testing system failed to capture the strain-softening process during relaxation tests in the post-failure region. The relaxation tests in the residual stage demonstrate a significant relaxation for failed rock. One specimen showed significant stress drop during relaxation tests, with around 20% of the stress relaxed within five hours. The ratio of relaxed stress to initial stress is very high.

In addition, one specimen failed during a relaxation test, implying that the strength was reduced during relaxation. It suggests that strength deterioration results from converting elastic strain to viscous strain or accumulating viscous strain. Figure 14A,B,C,D show an example of a relaxation test that occurred in the residual stage, with significant relaxation behavior similar to that before failure. The stress drop is quick at first and then gradually changes to a constant rate.

Simulation results

Equilibrium conditions

The simulation was run to equilibrium to simulate geostatic stresses in the numerical model accurately. The creep simulation was then activated from this state. Time-dependent deformation in the rock and the development of roof failure are driven by changes in stress distribution. This study investigates two parameters: plastic state and stress distribution at equilibrium. Figure 15A,B show the significant principal stress distribution and plastic state at equilibrium. High stress concentrations occur at entry corners, leading to shear failure onset. Directional in-situ horizontal stress increases stress concentrations at one corner, propagating failure towards the upper layers.

In reality, the zone size in Fig. 15 is approximately 0.5 m, a reasonable scale for simulating the large-scale behavior of the rock mass. A coarse mesh was used to capture the global behavior of the rock mass and study its time-dependent properties over a longer period. We have validated our model using fine-scale and coarse-scale simulations, and this discrepancy does not affect our results. The coarse-scale simulation was used to capture the global behavior of the rock mass, while the fine-scale simulation was used to validate the local behavior of the rock mass.

Constant viscous parameters

The numerical model with constant viscous parameters was run for a time equivalent to one day. Figure 16A,B show the significant principal stress distribution and failure condition, respectively. Comparing Figs. 15A and Fig. 16A reveals that the change in major principal stress distribution is insignificant, with more stress concentration occurring at the right edge of the entry. The change from Figs. 15A and 16A is a decrease in the magnitude of the stress. Additionally, comparing Figs. 15B and 16B shows no failure propagation occurs during creep model runs for one day. Therefore, the stress within the roof is relaxing, and there is no failure propagation when using constant viscous parameters (Fig. 16C).

Varying viscous parameters

The model's results differ significantly from those with constant parameters when using varying viscous parameters. The model advanced beyond equilibrium for one day. Comparing Figs. 14B and 17A shows that failure

Rock type	Test method	η_m (GPa*s)		E_k(GPa)		η_k(GPa*s)	
		Mean	Standard deviation	Mean	Standard deviation	Mean	Standard deviation
Sandy shale	Creep relaxation	2.32×10^{06} 2.05×10^{06}	1.19×10^{06} 6.59×10^{05}	72.92 106.54	33.43 24.89	9.15×10^{04} 8.94×10^{04}	2.84×10^{04} 3.62×10^{04}
limy shale	Creep relaxation	5.10×10^{05} 6.62×10^{05}	5.18×10^{05} 2.13×10^{05}	60.76 42.34	59.98 1.55	3.50×10^{04} 3.09×10^{04}	2.54×10^{04} 7.20×10^{03}
Shaly limestone	Creep	2.97×10^{06}	1.35×10^{06}	153.88	25.38	1.01×10^{05}	6.77×10^{04}
	Relaxation	8.25×10^{05}	1.06×10^{06}	80.17	96.32	5.99×10^{04}	6.00×10^{04}

Table 6. Mean and standard deviation of the viscous parameters.

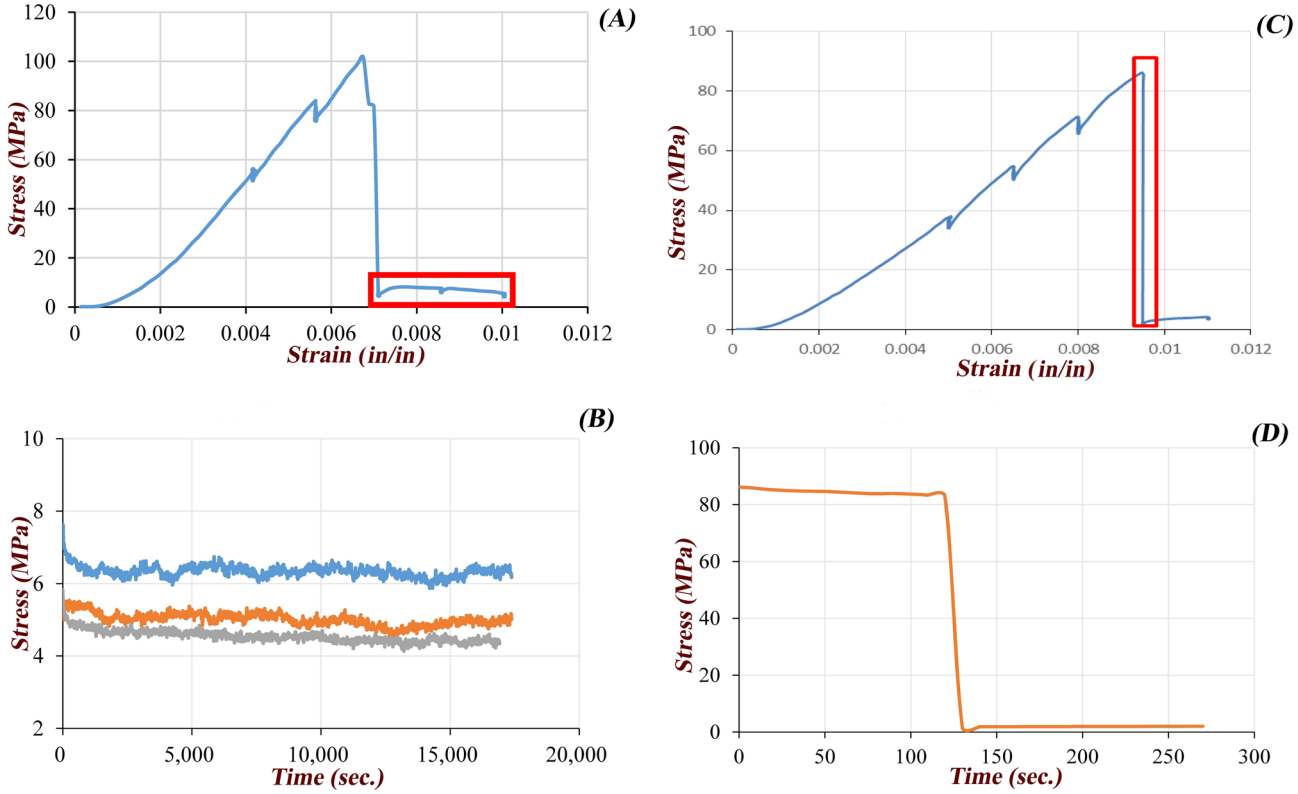

Figure 14. (**A**) Stress–strain curve, (**B**) Relaxation curves in the residual stage, (**C**) Stress–strain curve, (**D**) Relaxation curve including failure occurrence.

initiates from both edges of the entry, with failure propagating towards the upper strata from the right edge. The direction and range of the failure zone in Fig. 17A are similar to those of high-stress zones at equilibrium (marked in Fig. 14A). It indicates the extent of stress distribution on failure propagation over time.

Figure 17A shows that varying viscous parameters affect the stress distribution. In Fig. 14A, high-stress concentrations are observed above opening corners, while in Fig. 15A, these areas have very low stress after one day of creep simulation. Comparing Figs. 14A, 16A, and 17B shows that high-stress areas at equilibrium (Fig. 14A) already fail (Fig. 17A) and have low stress (Fig. 17B). Areas with high stress move deeper into the roof and surround areas with low stress.

The results demonstrate that areas with high stress at equilibrium gradually fail over time, and stress transfers from the failure zone to deeper solid rock. The observations also show that varying time-dependent parameters can result in different relaxation behaviors, leading to increased differential stress in surrounding elastic zones and failure potential (Fig. 17C).

Time-dependent property variation and roof failure

This study recognizes that standard specimen test results differ significantly from field measurements due to disparities in rock mass and block structure, joints, and fracture patterns. To address this issue, we incorporated time-dependent behavior into our numerical simulation using the Burgers model, which captures creep-induced failure and improves the accuracy of predicting time-dependent roof failure. We conducted laboratory-based rock displacement tests on coal samples from Iranian mines to validate our methodology. Our results demonstrate that incorporating strength degradation into numerical simulations can accurately predict failure under creep conditions and time-dependent roof failure. We propose implementing safety measures such as installing roof supports and monitoring systems to minimize the risk of roof collapses.

Our viscoelastic-plastic model simulates the time-dependent behavior of rock mass under various loading conditions, including creep and relaxation. The outcomes show that our approach can capture the gradual deterioration of rock mass strength over time, a critical factor in understanding roof stability in coal mines. The stress cloud map, an output of our model, provides valuable insights into the spatial distribution of stresses in the rock mass over time. Although not perfectly smooth, the map reflects the complexities of rock behavior under different loading conditions and can be used to identify areas of high-stress concentrations.

Our model also shows that the size of the plastic zone on the coal seam's roadway side can vary significantly depending on factors such as rock strength, confining pressure, and time-dependent properties. By simulating these factors, our model predicts a smaller or non-existent plastic zone in certain scenarios, highlighting the importance of considering these factors in modeling rock behavior.

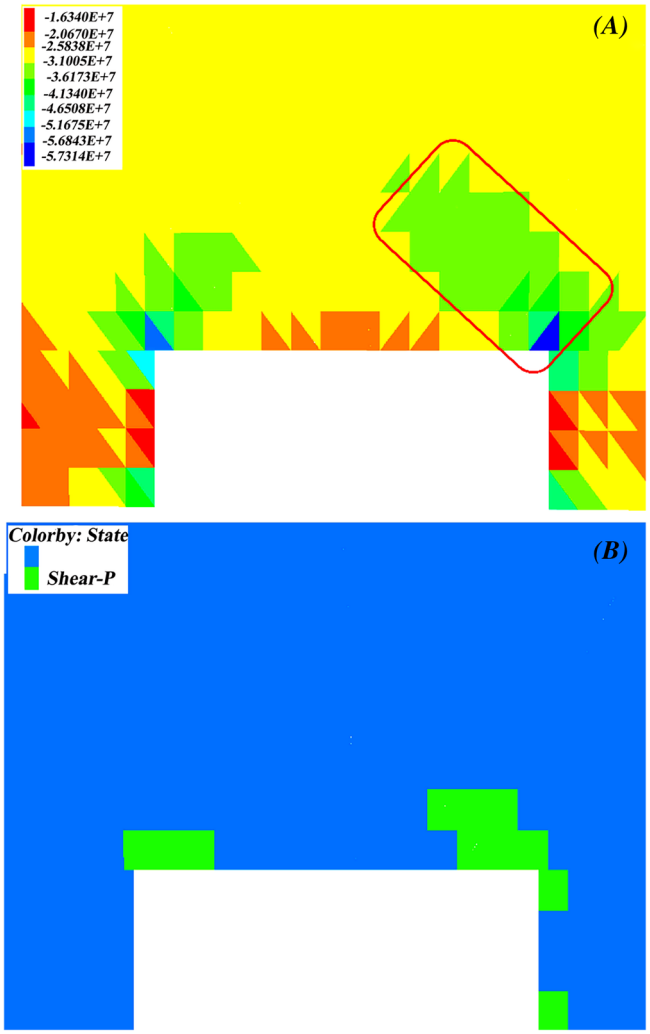

Figure 15. (**A**) Plot of major principal stress distribution at equilibrium (unit: Pascal), (**B**) Plot of plastic state at equilibrium.

In conclusion, our study demonstrates that our viscoelastic-plastic model can provide a more realistic representation of rock behavior under different loading conditions. It contributes to a better understanding of roof stability in coal mines and informs the development of strategies for improving roof stability and reducing the risk of roof collapses.

Limitations and highlights of the study

Limitations

1. The laboratory-based rock displacement testing may not accurately represent real-world conditions.
2. The results are specific to Iran's coal mines, and the applicability to other regions or rock types is uncertain.
3. The study did not consider other factors influencing roof stability, such as geological structure, mining method, and environmental conditions.

Highlights

1. Rock masses with high stress at equilibrium gradually fail over time, and stress is transferred to deeper solid rock.
2. Varying viscous parameters lead to distinct relaxation behaviors and stress distributions.
3. Incorporating strength degradation into numerical simulations improves accuracy in predicting time-dependent roof failure under creep conditions.

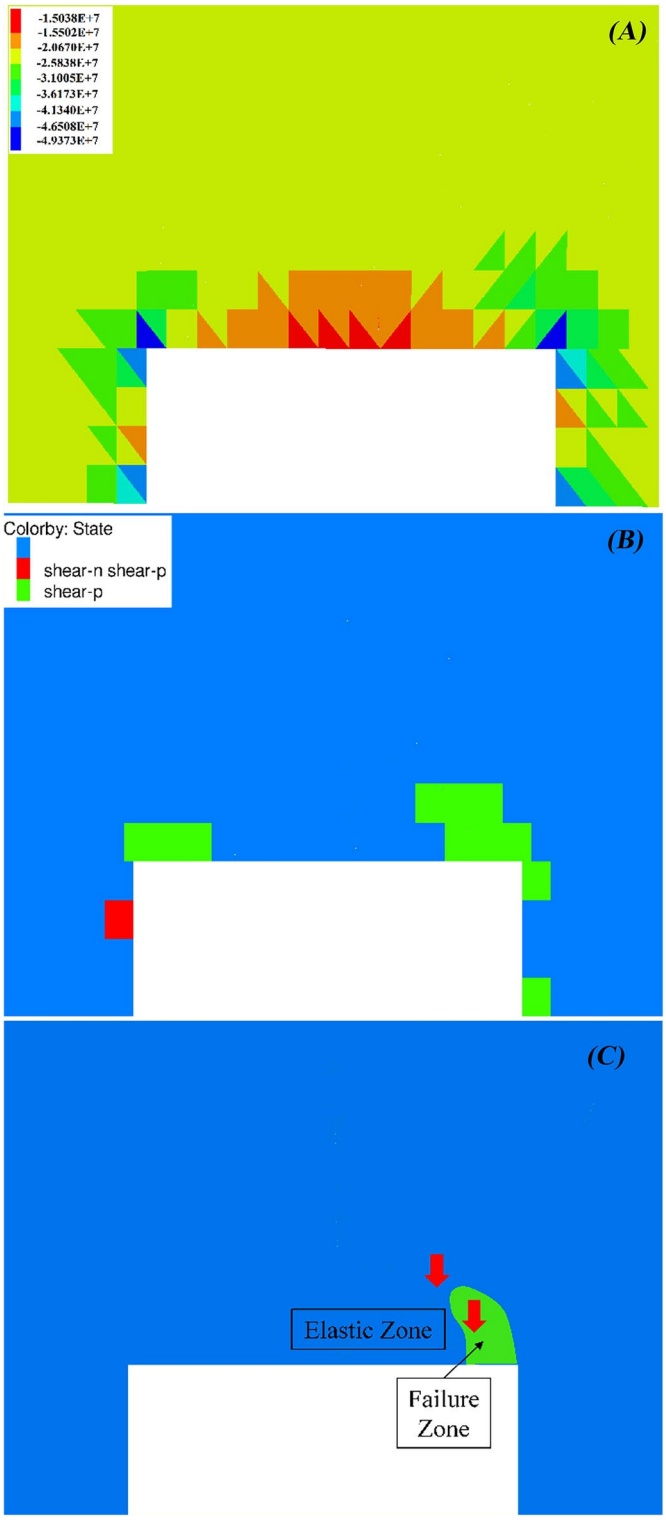

Figure 16. (**A**) Plot of major principal stress distribution after one day for model with constant viscous parameters (unit: Pascal), (**B**) Plot of plastic state after one day for model with constant viscous parameters, (**C**) "synchronized" stress relaxation in plastic and elastic zone for the model with constant viscous parameters.

4. Rock displacement testing can assess coal mine roof stability by measuring the reduction in roof resistance over time.

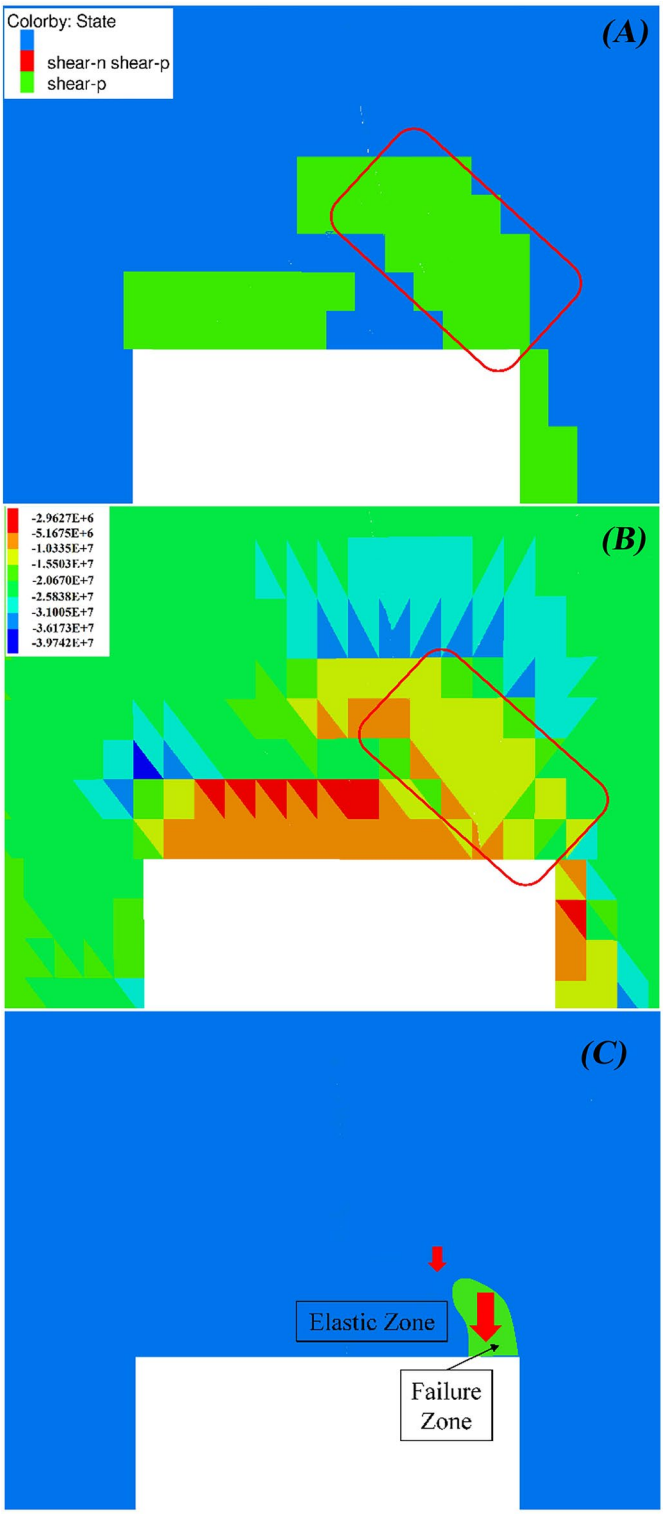

Figure 17. (**A**) Plot of plastic state distribution after one day for model with varying viscous parameters, (**B**) Plot of major principal stress after one day for model with varying viscous parameters (unit: Pascal), (**C**) stress relaxation in plastic and elastic zone for the model with varying viscous parameters.

5. The study provides valuable insights into the time-dependent behavior of rock masses in Iranian coal mines, informing strategies for improving roof stability and reducing the risk of roof collapses.

Discussion

Mechanism for time-dependent propagation of failure

The primary objective of this study is to quantify the time-dependent characteristics of rock masses in Iranian coal mines and their impact on roof resistance reduction. By subjecting rock samples to varying stress levels over time, researchers can simulate the gradual deterioration of rock strength in underground mining conditions. It allows them to monitor the displacement of rock samples and assess the effects of roof resistance reduction on roof stability.

The mechanism of time-dependent failure propagation is thoroughly investigated using a robust numerical model. Figure 18 illustrates the failure process, which begins with stress redistribution triggered by excavation, culminating in shear failure at the roof, particularly at entry corners. The difference in time-dependent properties between intact and failed rock causes failed rock to relax stress faster than intact rock. The surrounding rock remains elastic and responds accordingly. However, rapid stress relaxation in the adjacent failure zone reduces confinement to the surrounding rock, leading to increased differential stress, particularly at the boundary between the failure and elastic zones.

If the time-dependent differential stress exceeds the rock strength, failure can occur at the boundary of the failure zone, resulting in time-dependent failure propagation.

Our modeling results show that several factors influence time-dependent failure propagation. Firstly, the disparity in time-dependent properties between intact and failed rock affects the failure process. No failure propagation occurred when using constant viscous parameters, but failure propagated using varying viscous parameters for intact and failed rock.

Secondly, the initial condition for time-dependent failure is determined by the failure zone at equilibrium. The failure zone initiates at entry corners due to stress redistribution during entry development. Our modeling results show that high differential stress builds up at the boundary between the failure and elastic zones, causing time-dependent failure to begin propagating from this boundary.

Lastly, in-situ stress is crucial in determining the location and direction of time-dependent failure propagation. In-situ stress can influence the formation of a failure zone during entry development and guide the direction of time-dependent failure propagation. In-situ stress governs stress distribution around an opening, identifying high-stress zones where differential stress is more likely to exceed rock strength and trigger failure. Consequently, time-dependent failure tends to propagate along the path of high major principal stress.

Influence of failure propagation on roof convergence

This study examined the impact of failure propagation on roof convergence by comparing models with constant and varying parameters. The results in Fig. 19 show that the difference between the curves increases over time, indicating a time-dependent failure propagation process. The figure also presents the plastic state of the model at different times with varying parameters. After the initial stage, the convergence curve with varying parameters exhibits a steeper slope as failure propagation continues. In contrast, the curve with constant parameters shows a relatively constant rate with minor fluctuations in the secondary stage.

Influence of strength degradation on time-dependent roof failure

This section examines the built-in constitutive model in 3DEC 7.0 software, which combines creep models and the Mohr–Coulomb failure criterion. The model does not account for strength degradation, and rock failure occurs only when the stress meets the failure criterion. In contrast, the 3DEC 7.0 viscoelastic-plastic model, which combines the Burgers model and the Mohr–Coulomb failure criterion, was used to simulate an unconfined creep test. The simulation applied a constant stress of 98% of the strength to the top of the specimen and ran to equilibrium before simulating creep for 2 million seconds (555.6 h). As shown in Fig. 20A,B, the specimen deformed without failure, with an axial viscous strain approximately 17 times greater than the instantaneous elastic strain.

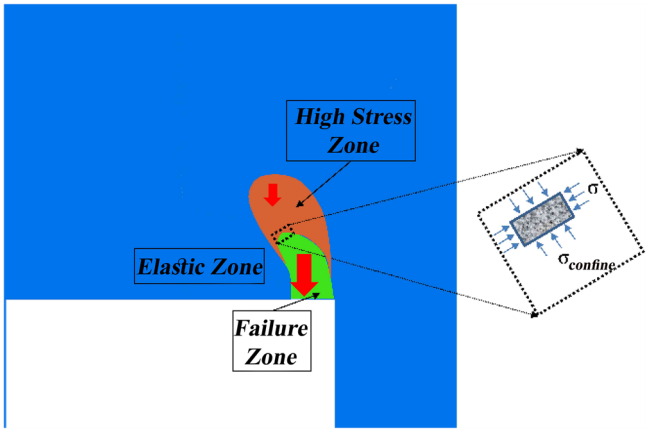

Figure 18. Illustration of mechanism for time-dependent propagation of failure.

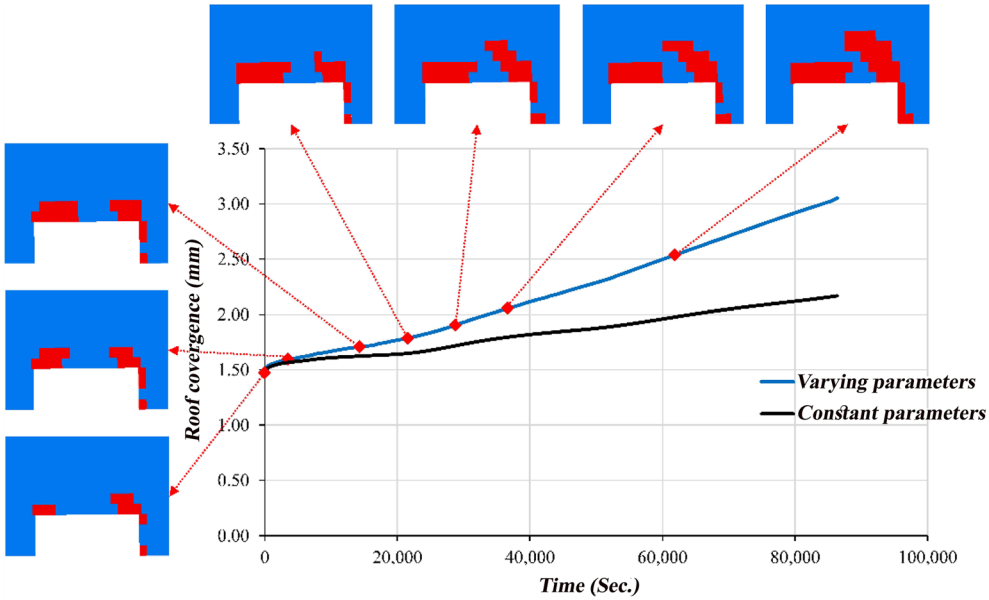

Figure 19. Comparison of roof convergence for the models with constant and varying parameters.

However, this result differs from laboratory test results. Studies should consider strength degradation induced by viscous deformation to capture rock failure under creep conditions. The effective viscous strain is a parameter that quantifies damage caused by viscous behavior and can be linked to rock strength, similar to effective shear plastic strain in strain softening models. This parameter allows strength degradation caused by viscous deformation to be considered for complex stress conditions and incorporated into numerical simulations.

Incorporation of strength degradation into numerical simulation

Incorporating strength degradation into numerical simulations is crucial for accurately modeling rock behavior. Laboratory creep tests provide valuable information on the relationship between strength degradation and stress levels. By conducting unconfined creep tests at various stress levels until specimen failure, the accumulated effective viscous strain and corresponding strength values after degradation can be determined. The Burgers model calculates the accumulated effective viscous strain at each stress level.

A FISH function was developed to implement strength degradation during time-dependent simulations in 3DEC 7.0. The cvis model, which incorporates the Burgers model for time-dependent behavior and the Mohr–Coulomb criterion for failure prediction, represents the time-dependent behavior of rock. At each time step, the FISH function calculates the accumulated effective viscous strain and updates strength values, assuming a constant cohesion value and decreasing friction angle with increasing viscous strain.

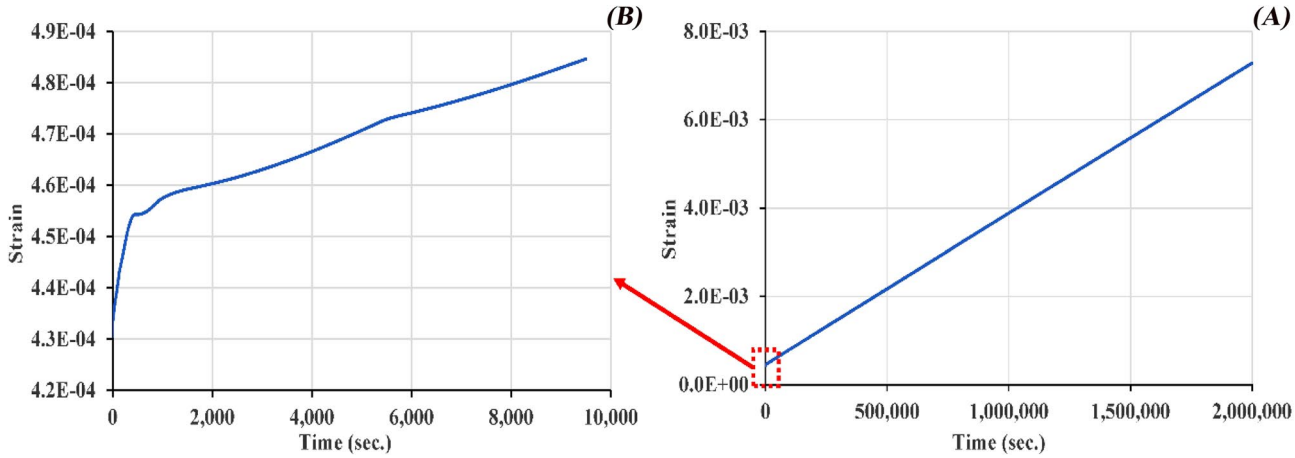

Figure 20. Stress–strain curve for the simulated unconfined creep test with Burgers model and Mohr–Coulomb Criterion as (**A**) full graph, (**B**) magnified graph.

The relationship between strength value and effective viscous strain was converted to a relationship between friction angle and effective viscous strain (Fig. 21A,B). As effective viscous strain accumulates over time, the friction angle gradually decreases, leading to strength degradation. A single unconfined creep test was simulated to verify the simulation method. Figure 21B illustrates the strength degradation relation represented by the relationship between friction angle and effective viscous strain.

During a creep test, the effective viscous strain accumulates over time, leading to decreasing strength values until specimen failure occurs when the strength value equals the applied constant stress (Fig. 21C). The simulated specimen exhibited typical creep behavior characterized by primary, secondary, and tertiary stages. The accelerating strain rate in the tertiary stage indicated specimen failure, which occurred after some time during the creep test.

Numerical study on the influence of strength degradation on roof behavior

This study investigates the impact of strength degradation on roof behavior using the 3DEC 7.0 program, where the FISH function controls strength degradation during time-dependent simulations. The parameters used in the simulations are presented in Table 2 and Fig. 21B. In contrast, the model employed for the simulations is shown in Fig. 8. Two models were utilized: one featuring constant viscous parameters to account for strength degradation, and another incorporating varying viscous parameters to account for both strength degradation and time-dependent property variation.

The Burgers model accurately describes elastic behavior under hydrostatic and deviatoric stress conditions, with time-dependent behavior only occurring under deviatoric stress. Figure 22A shows the distribution of deviatoric stress, which reveals an arch-shaped area with high deviatoric stress within the roof. This area also exhibits high maximum shear stress, as depicted in Fig. 22B, a crucial indicator of the Mohr–Coulomb failure criterion. The similarity between the distributions of deviatoric stress and maximum shear stress suggests that the arch-shaped area experiences high deviatoric stress and high maximum shear stress, implying that large time-dependent deformation and strength degradation are likely to occur.

Notably, the time-dependent simulation, which was activated and ran for one day after reaching equilibrium conditions, revealed significant findings. Figure 23A,B,C depict the failure condition, effective viscous strain distribution, and friction distribution within the roof, respectively. A comparison between the failure condition in Figs. 15B and 23B show minor changes, with slight failure propagation observed above the left entry corner. The use of constant viscous parameters in the simulation led to a relaxation of stress in the failure zone and surrounding elastic zone at the same rate. Strength degradation occurred gradually with accumulated viscous strain, particularly within the arch-shaped area, as shown in Fig. 23B,C. The rocks' stress relaxed as a result of viscous deformation, leading to a reduction in rock strength coinciding with decreased stress. This prevented failure propagation over time. Additionally, running the model with constant viscous parameters for an extra 30 days did not result in failure propagation over a month under these simulation conditions, further highlighting the robustness of the findings. In conclusion, Fig. 24A,B illustrate the plastic states after two minutes and one day, respectively, for the model with varying viscous parameters. This study initially investigated the impact of varying viscous parameters on models with strength degradation. Comparing Figs. 22A,B, and 24A, failures originating from equilibrium entry corners propagate rapidly along areas of high deviatoric stress and maximum shear stress, coalescing within two minutes. The failure zone expands gradually, resulting in a significantly larger zone than the constant-viscous-parameter model.

The critical difference between these models lies in the viscous parameters in the post-failure region. As a result, stress relaxation rates varied inside and outside the failure zone due to the distinction in viscous parameters between intact and failed rock. This amplifies the stress difference at the boundary between the failure and elastic zones, potentially facilitating failure propagation. The increasing stress difference also accelerates strength degradation, further promoting failure propagation.

Our study also examined the influence of strength degradation on models with varying viscous parameters, providing practical implications for the field of geotechnical engineering. The difference in plastic states depicted in Figs. 17A and 24B can be attributed to strength degradation. In Fig. 17A, where the model did not account for strength degradation, failures originating from the two entry corners propagated separately towards the upper strata. However, when strength degradation was considered, the plastic states in Fig. 24a,b demonstrate that failures coalesced first before propagating upwards, resulting in a larger failure zone. Therefore, considering strength degradation altered the failure process and increased the failure zone, a crucial finding for engineers and professionals in the field.

The grids displayed in Figs. 23 and 24 demonstrate that they can better showcase the expansion characteristics of the plastic zone surrounding the roadway due to their ability to provide a visual representation of how the rock deforms and expands in response to mining activities over time. In contrast, the contour plot in Fig. 19 shows the deformation scale, an essential aspect of understanding the time-dependent behavior of the rock mass.

In other words, Figs. 23 and 24 provide a spatial visualization of the plastic zone expansion, which is not explicitly shown in Fig. 19. The contour plot in Fig. 19 displays the magnitude of deformation. However, it does not provide information on the spatial distribution of deformation, which is crucial for understanding the expansion characteristics of the plastic zone.

The instantaneous elastic strain was 4.35×10^{-4}, and creep simulation was activated to run for a time equivalent to 2×10^{6} s. The results show that areas with high stress at equilibrium gradually fail over time and the stress transfers from the failure zone into deeper solid rock. The study demonstrates that varying viscous parameters can lead to different relaxation behaviors and stress distributions.

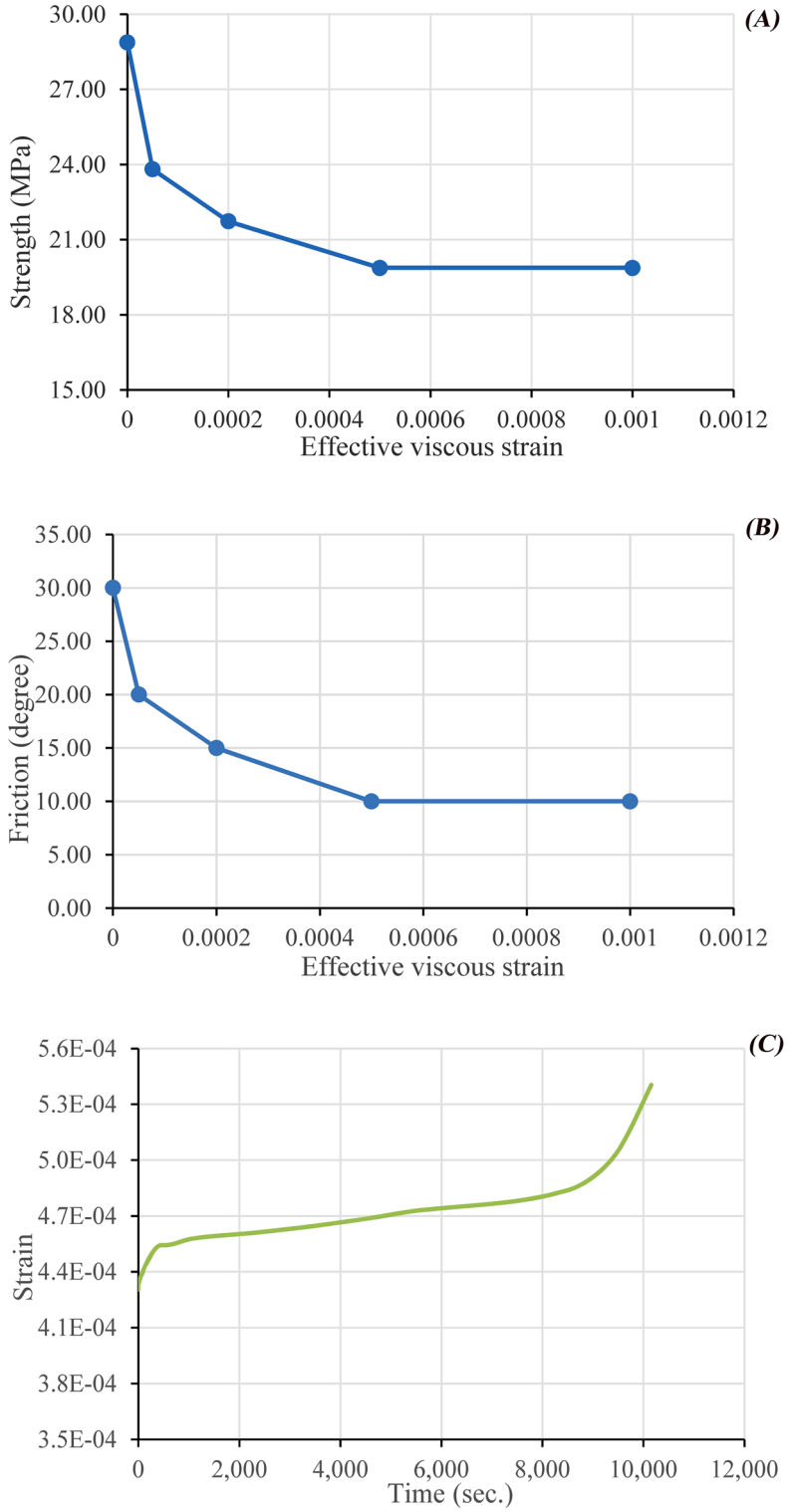

Figure 21. (**A**) Strength degradation relation, (**B**) Relation between friction angle and effective viscous strain used in the simulation, (**C**) Creep curve showing three stages for the specimen considering strength degradation.

Rock mass behavior around roadway excavation

This study uses rock displacement testing to investigate the impact of time-dependent characteristics on roof resistance reduction in Iran's coal mines. It proposes a new constitutive model incorporating rock behavior,

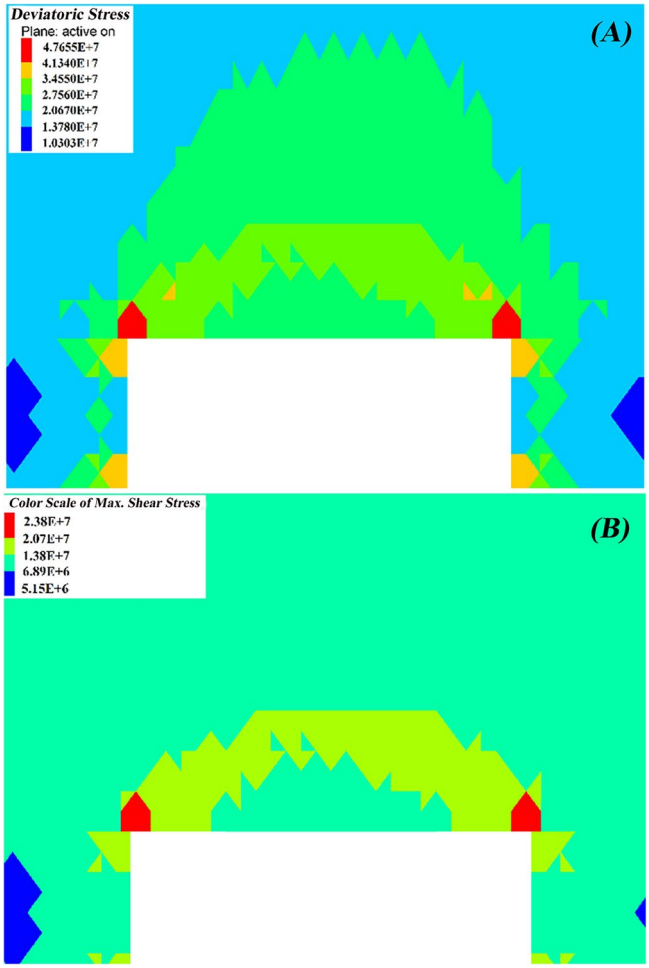

Figure 22. (**A**) Plot of deviatoric stress distribution at equilibrium, (**B**) Plot of maximum shear stress distribution at equilibrium (Units: Pascal).

including time-dependent behavior, strain-softening, and strength deterioration. To discuss the results, we have provided a numerical contour of the rock mass's initial damage and stress distribution after the equilibrium of the numerical model construction and calculation of the roadway excavation.

Initial damage distribution (After equilibrium)
The rock mass around the roadway exhibits high-stress concentrations, with a maximum stress value of 30 MPa. The damage distribution shows a gradual failure zone with a radius of approximately 5 m from the roadway, characterized by micro-cracking and shear failure.

Stress distribution
The stress distribution shows a significant decrease in stress values within the damage zone, with a minimum value of 10 MPa. Outside the damage zone, the stress gradient remains relatively constant, ranging from 20 to 30 MPa. The maximum stress value occurs at the boundary between the damage zone and the undamaged rock.

Damage parameters
Damage fraction: 0.2–0.5
Damage type: Micro-cracking and shear failure.
Damage radius: approximately 5 m.
The study's numerical analysis reveals that the rock mass around the roadway exhibits significant stress concentrations and a damage zone with a radius of approximately 5 m, characterized by micro-cracking and shear failure. The findings provide valuable insights into the behavior of the rock mass around roadway excavation in Iran's coal mines, informing the development of more accurate predictive models for roof resistance reduction and potential rock stability issues.

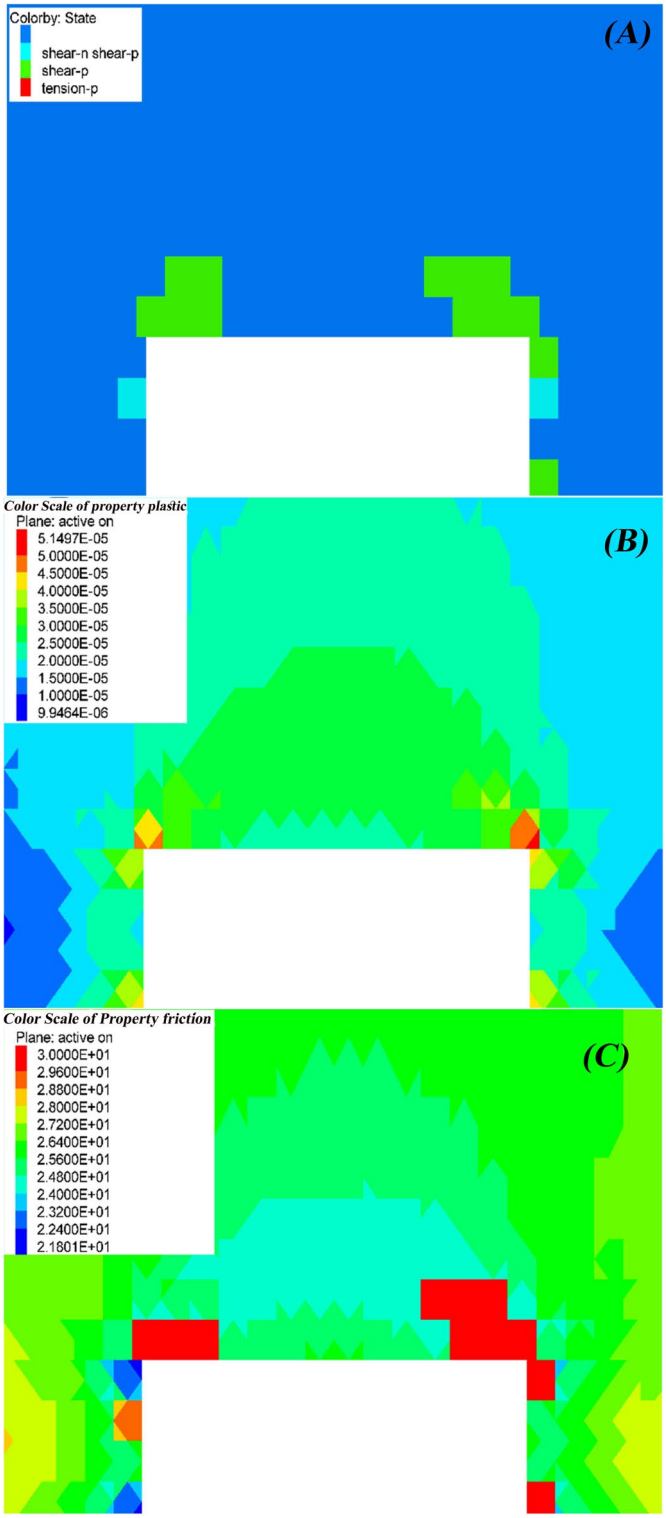

Figure 23. (**A**) Plot of plastic state after one day for model with constant viscous parameters and strength degradation, (**B**) Plot of effective viscous strain distribution after one day for the model with constant viscous parameters and strength degradation, (**C**) Plot of friction angle after one day for the model with constant viscous parameters and strength degradation (Unit: degree).

Application of viscoelastic-plastic model

To demonstrate the application of the viscoelastic-plastic model to coal mine roadway engineering, we consider

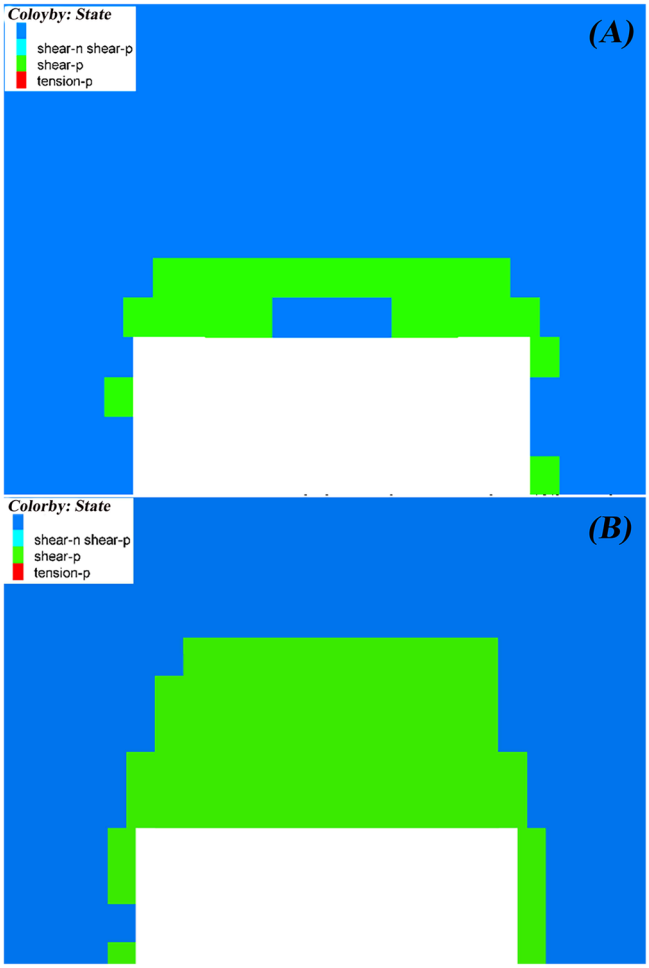

Figure 24. (**A**) Plot of plastic state after two minutes for the model with varying parameters and strength degradation, (**B**) Plot of plastic state after one day for model with varying parameters and strength degradation.

a 500-m-deep coal mine in Iran with sedimentary rocks as the overburden, having a Young's modulus of 10 GPa and a Poisson's ratio of 0.3. The coal seam is 3 m thick, with a Young's modulus of 5 GPa and a Poisson's ratio of 0.2. The model simulates the time-dependent behavior of the rock mass above the coal seam and predicts the reduction in roof resistance over time due to creep and relaxation processes.

The results show that roof resistance decreases by approximately 20% over ten years due to creep and relaxation processes, increasing the risk of roof collapse. This reduction in roof resistance can be mitigated by implementing more effective support systems or adjusting the mining sequence. The findings of this study inform strategies to optimize coal seam mining operations and mitigate roadway instability risks.

Scenario example

To further illustrate the application, let us consider a specific scenario: simulating the behavior of a 10-m-high coal mine roof over two years with an initial stress level of 0.5 MPa. According to the viscoelastic-plastic model, the stress level would decrease to 0.4 MPa after one year and 0.3 MPa after two years, indicating significant strength degradation.

This study provides valuable insights into the time-dependent behavior of rock mass in coal mines, contributing to developing strategies for improving roof stability and reducing the risk of roof collapses. Its application can lead to improved safety measures and reduced risk in coal mines, ultimately ensuring a safer working environment for miners.

Validating numerical simulations with measured data

Rock mass behavior exhibits significant time-dependent characteristics, with stress relaxation occurring rapidly in the post-failure region. Numerical simulations and laboratory tests demonstrate that the Burgers model accurately captures this behavior, showing good agreement with experimental results. As a result, the rock's strength is expected to decrease over time, with a more pronounced reduction in strength observed in the post-failure region.

The study's findings significantly affect improving safety measures and risk management practices in Iran's coal mines. For example, the results show that relaxation behaviors in sandstone specimens from coal mines depend on the initial stress condition, with failed specimens relaxing more than intact ones. Two key factors contribute to stepwise relaxation behavior: the propagation of non-persistent failure planes during stress relaxation and the shear-off of asperities along the major failure plane.

Over time, the rock mass's stress distribution is expected to change, with a greater stress concentration in the post-failure region. The predicted failure pattern suggests that the rock mass will fail stepwise, with multiple failure planes propagating through the rock. Numerical simulations have been validated by comparing results with measured engineering data from laboratory tests, demonstrating good agreement and confirming the accuracy of predictions.

The study highlights the importance of considering time-dependent behavior when predicting rock mass strength and failure patterns. The findings emphasize the necessity of accurately modeling viscoelastic-plastic behavior to ensure safe and efficient mining operations.

While our study has limitations due to coarse mesh size and limited data availability, it provides a valuable preliminary understanding of coal mine roof stability. Future studies can build upon our findings by incorporating more detailed data and advanced numerical methods. For instance, collecting accurate data on rock mass properties and excavation conditions could refine our understanding of the system's behavior. Advanced methods like finite element or discontinuous Galerkin could also provide a more accurate representation of rock mass behavior.

The use of 3DEC software for simulating the behavior of a rock mass is widely accepted in the field of rock mechanics. However, it is acknowledged that the numerical model's performance depends on the mesh size. To validate our simulation, we conducted a sensitivity analysis to assess the effect of mesh size on the predicted results. Our findings indicate that a mesh size of 0.5 m reasonably balances accuracy and computational efficiency.

As shown in Table 7, a mesh size of 0.5 m yields an error of approximately 6.1%, which is considered acceptable for this type of simulation. Therefore, we recommend using a mesh size of 0.5 m for future simulations to predict rock displacement and stability. To further investigate the impact of mesh size on predicted rock behavior, we conducted multiple simulations with varying mesh sizes, ranging from 0.1 to 2.0 m.

Table 8 presents the results, which show that as the mesh size decreases, the mean absolute error (MAE) in displacement decreases, indicating more accurate predictions at smaller mesh sizes. The coefficient of determination (R^2) also increases as the mesh size decreases, indicating a better fit of the model to the experimental data. Based on these results, we recommend using a mesh size of less than or equal to 0.5 m for accurate rock displacement and stability predictions in this specific application.

In conclusion, our study highlights the importance of considering time-dependent behavior when predicting rock mass strength and failure patterns. The findings have significant implications for improving safety measures and risk management practices in Iran's coal mines. Future research should focus on refining our understanding of rock mass behavior using more detailed data and advanced numerical methods to ensure safe and efficient mining operations.

Mesh size (m)	Rock displacement (mm)	Error (%)
0.1	10.5	12.5
0.2	10.2	10.1
0.3	9.8	8.5
0.4	9.5	7.3
0.5	9.2	6.1
1.0	8.8	4.4
2.0	6.5	4

Table 7. Influence of mesh size on predicted rock displacement.

Mesh size (m)	Mean absolute error (MAE) in rock displacement (mm)	Coefficient of determination (R^2)
0.1	0.08 ± 0.02	0.90 ± 0.03
0.2	0.12 ± 0.03	0.85 ± 0.05
0.3	0.18 ± 0.04	0.80 ± 0.06
0.4	0.24 ± 0.05	0.75 ± 0.07
0.5	0.29 ± 0.06	0.70 ± 0.08
1.0	0.60 ± 0.12	0.55 ± 0.10
1.5	1.10 ± 0.20	0.40 ± 0.15
2.0	1.80 ± 0.30	0.25 ± 0.20

Table 8. Sensitivity analysis of mesh size on predicted rock displacement using statistical approaches.

Conclusions and recommendations

This study investigates the impact of time-dependent characteristics on roof resistance reduction in Iran's coal mines. The results show that incorporating strength degradation into numerical simulation can capture the failure under creep conditions and improve the accuracy of predicting time-dependent roof failure. The study proposes developing safety measures such as installing roof supports and monitoring systems to minimize the risk of roof collapses. The Burgers model is introduced as a critical tool for determining time-dependent parameters, and a novel fitting procedure is proposed to simplify the process.

Key findings

- Time-dependent characteristics affect roof resistance reduction in coal mines, and incorporating strength degradation into numerical simulation can improve the accuracy of predicting time-dependent roof failure.
- The Burgers model is a suitable tool for determining time-dependent parameters, and a novel fitting procedure is proposed to simplify the process.
- Relaxation tests can be used to study the time-dependent properties of rock in the pre-failure region, and the results can be used to determine the parameters of the Burgers model.
- The relaxation test can be extended to the post-failure region by performing relaxation tests on specimens that have failed under uniaxial compression.

Based on research results, we propose the following specific recommendations for improvement:

- Incorporate time-dependent characteristics into numerical simulations using advanced models, such as the Burgers model, to account for viscoelastic-plastic behavior, considering bedding planes and roof support.
- Develop a new constitutive model incorporating all relevant features, including time-dependent behavior before and after failure, strain-softening behavior, and strength deterioration.
- Conduct laboratory-based rock displacement testing to evaluate roof stability and resistance reduction by testing rock samples under varying stress levels.
- Implement more effective roof support systems, monitoring techniques, and strategies for mitigating the impact of time-dependent characteristics on roof stability in coal mines.
- Utilize advanced numerical methods to simulate complex rock behavior and develop more accurate predictions, collaborating with industry experts to develop practical solutions for improving roof stability.

These recommendations focus on the most critical areas of improvement, combining related items and eliminating unnecessary words to provide a concise and clear direction for researchers to improve their understanding of time-dependent dynamics in coal mine roof stability.

Data availability

The datasets generated during and/or analysed during the current study are available from the corresponding author on reasonable request.

Received: 27 May 2024; Accepted: 9 August 2024
Published online: 22 August 2024

References

1. Zhao, Y., Zhang, N. & Wang, J. Failure properties of roadway with extra-thick coal seams and its control techniques. *Heliyon* **10**(1), e23990. https://doi.org/10.1016/j.heliyon.2024.e23990 (2024).
2. Zhang, C., Chen, Y., Ren, Z. & Wang, F. Compaction and seepage characteristics of broken coal and rock masses in coal mining: A review in laboratory tests. *Rock Mech. Bull.* **3**(2), 100102. https://doi.org/10.1016/j.rockmb.2024.100102 (2024).
3. Xie, Z. *et al.* Model experiment research on HPTL anchoring technology for coal-rock composite roof in deep roadway. *Sci. Rep.* **13**(1), 2381. https://doi.org/10.1038/s41598-023-29232-5 (2023).
4. Li, J. *et al.* Study on deformation and instability characteristics and control technology of deep soft rock roadway with strong mining. *SN Appl. Sci.* **5**(11), 292. https://doi.org/10.1007/s42452-023-05516-3 (2023).
5. Hosseini, N. Evaluation of the rockburst potential in longwall coal mining using passive seismic velocity tomography and image subtraction technique. *J. Seismol.* **21**(5), 1101–1110. https://doi.org/10.1007/s10950-017-9654-4 (2017).
6. Pirhadi, A., Kianoush, P., Ebrahimabadi, A. & Shirinabadi, R. Wellbore stability in a depleted reservoir by finite element analysis of coupled thermo-poro-elastic units in an oilfield, SW Iran. *Results Earth Sci.* **1**, 100005. https://doi.org/10.1016/j.rines.2023.100005 (2023).
7. Kianoush, P. *et al.* Formation pressures determination utilizing the integration of fractal and geostatistical modelling in a hydrocarbon formation of SW Iran. *J. Anal. Numer. Methods Min. Eng.* **14**(39), 1590. https://doi.org/10.22034/anm.2024.19796.1590 (2024b).
8. Kianoush, P. *et al.* Hydrogeological studies of the Sepidan basin to supply required water from exploiting water wells of the Chadormalu mine utilizing reverse osmosis (RO) method. *Results Earth Sci.* **2**, 100012. https://doi.org/10.1016/j.rines.2023.100012 (2024a).
9. Molinda, G. & Mark, C. Ground failures in coal mines with weak roof. *Electron. J. Geotech. Eng.* **15**, 1–42 (2010).
10. Dang, J., Tu, M., Zhang, X. & Bu, Q. Research on the bearing characteristics of brackets in thick hard roof mining sites and the effect of blasting on roof control. *Geomech. Geophys. Geo-Energy Geo-Resour.* **10**(1), 18. https://doi.org/10.1007/s40948-024-00735-3 (2024).
11. Kianoush, P. Additional Exploration of Ground Water Resources at Sangan Plain in Khaf For Water Supply at Sangan Iron Ore Project by Computerized Model, Master of Science in Mining Engineering, Thesis, Master of Science in Mining Engineering,

Petroleum and Mining Engineering, Islamic Azad University, South Tehran Branch, 280, https://doi.org/10.13140/RG.2.2.28658.27846 (2005).
12. Rong, H. *et al.* Research on rockburst prevention systems based on the attenuation law of coal and rock vibration wave energy. *Sci. Rep.* **14**(1), 6452. https://doi.org/10.1038/s41598-024-57258-w (2024).
13. Kianoush, P. *et al.* ANN-based estimation of pore pressure of hydrocarbon reservoirs—A case study. *Arab. J. Geosci.* **16**(5), 302. https://doi.org/10.1007/s12517-023-11373-6 (2023c).
14. Kianoush, P., Mohammadi, G., Hosseini, S. A., Khah, K. F. & N. & Afzal, P.,. Determining the drilling mud window by integration of geostatistics, intelligent, and conditional programming models in an oilfield of SW Iran. *J. Petrol. Explor. Prod. Technol.* **13**(6), 1391–1418. https://doi.org/10.1007/s13202-023-01613-6 (2023).
15. Saffari, M., Ameri, M., Jahangiri, A. & Kianoush, P. Development of rheological models depending on the time, temperature, and pressure of wellbore cement compositions: A case study of southern Iran's exploratory oilfields. *Arab. J. Geosci.* **17**(6), 175. https://doi.org/10.1007/s12517-024-11982-9 (2024).
16. Kianoush, P., Mohammadi, G., Hosseini, S. A., Khah, N. K. F. & Afzal, P. Inversion of seismic data to modeling the Interval Velocity in an Oilfield of SW Iran. *Results Geophys. Sci.* **13**, 100051. https://doi.org/10.1016/j.ringps.2023.100051 (2023).
17. Hosseini, S. A., Khah, K. F. & N., Kianoush, P., Afzal, P., Shakiba, S. & Jamshidi, E.,. Boundaries determination in potential field anomaly utilizing analytical signal filtering and its vertical derivative in Qeshm Island SE Iran. *Results Geophys. Sci.* **14**, 100053. https://doi.org/10.1016/j.ringps.2023.100053 (2023).
18. Khah, N. K. F., Salehi, B., Kianoush, P. & Varkouhi, S. Estimating elastic properties of sediments by pseudo-wells generation utilizing simulated annealing optimization method. *Results Earth Sci.* **2**, 100024. https://doi.org/10.1016/j.rines.2024.100024 (2024).
19. Hosseini, S. A., Khah, K. F. & N., Kianoush, P., Arjmand, Y., Ebrahimabadi, A. & Jamshidi, E.,. Tilt angle filter effect on noise cancelation and structural edges detection in hydrocarbon sources in a gravitational potential field. *Results Geophys. Sci.* **14**, 100061. https://doi.org/10.1016/j.ringps.2023.100061 (2023).
20. Shirinabadi, R., Moosavi, E. & Gholinejad, M. Application of distinct element method to analyze the fracture and in-situ stress on wellbore stability under triaxial compression. *Indian Geotech. J.* **51**(6), 1384–1398. https://doi.org/10.1007/s40098-021-00549-0 (2021).
21. Hosseini, S. A. *et al.* Integration of fractal modeling and correspondence analysis reconnaissance for geochemically high-potential promising areas, NE Iran. *Results Geochem.* **11**, 100026. https://doi.org/10.1016/j.ringeo.2023.100026 (2023).
22. Xu, J. *et al.* Deformation and damage dynamic characteristics of coal–rock materials in deep coal mines. *Int. J. Damage Mech.* **28**(1), 58–78. https://doi.org/10.1177/1056789517741950 (2017).
23. Sun, Y., Li, G. & Zhang, J. Investigation on jet grouting support strategy for controlling time-dependent deformation in the roadway. *Energy Sci. Eng.* **8**(6), 2151–2158. https://doi.org/10.1002/ese3.654 (2020).
24. Kianoush, P. *et al.* Geobody estimation by Bhattacharyya method utilizing nonlinear inverse modeling of magnetic data in Baba-Ali iron deposit, NW Iran. *Heliyon* **9**(11), e21115. https://doi.org/10.1016/j.heliyon.2023.e21115 (2023).
25. Alejano, L. R. & Alonso, E. Considerations of the dilatancy angle in rocks and rock masses. *Int. J. Rock Mech. Min. Sci.* **42**(4), 481–507. https://doi.org/10.1016/j.ijrmms.2005.01.003 (2005).
26. Yang, S.-Q. *et al.* Three-dimensional failure behavior and cracking mechanism of rectangular solid sandstone containing a single fissure under triaxial compression. *Rock Mech. Bull.* **1**(1), 100008. https://doi.org/10.1016/j.rockmb.2022.100008 (2022).
27. Saber, E., Qu, Q., Aminossadati, S. M., Zhu, Y. & Chen, Z. Horizontal borehole azimuth optimization for enhanced stability and coal seam gas production. *Rock Mech. Bull.* **3**(1), 100100. https://doi.org/10.1016/j.rockmb.2023.100100 (2024).
28. Eftekhari, S. H., Memariani, M., Maleki, Z., Aleali, M. & Kianoush, P. Electrical facies of the Asmari Formation in the Mansouri oilfield, an application of multi-resolution graph-based and artificial neural network clustering methods. *Sci. Rep.* **14**(1), 5198. https://doi.org/10.1038/s41598-024-55955-0 (2024b).
29. Eftekhari, S. H., Memariani, M., Maleki, Z., Aleali, M. & Kianoush, P. Hydraulic flow unit and rock types of the Asmari Formation, an application of flow zone index and fuzzy C-means clustering methods. *Sci. Rep.* **14**(1), 5003. https://doi.org/10.1038/s41598-024-55741-y (2024).
30. Peng, S. S. Time-dependent aspects of rock behavior as measured by a servocontrolled hydraulic testing machine. *Int. J. Rock Mech. Min. Sci. Geomech. Abstr.* **10**(3), 235–246. https://doi.org/10.1016/0148-9062(73)90033-8 (1973).
31. Kaiser, P. K. & Morgenstern, N. R. Phenomenological model for rock with time-dependent strength. *Int. J. Rock Mech. Min. Sci. Geomech. Abstr.* **18**(2), 153–165. https://doi.org/10.1016/0148-9062(81)90740-3 (1981).
32. Swanson, P. L. Subcritical crack growth and other time- and environment-dependent behavior in crustal rocks. *J. Geophys. Res.: Solid Earth* **89**(B6), 4137–4152. https://doi.org/10.1029/JB089iB06p04137 (1984).
33. Dusseault, M.B. & Fordham, C.J. 6 - Time-dependent Behavior of Rocks. in *Rock Testing and Site Characterization* (ed. Hudson, J.A.) 119–149. https://doi.org/10.1016/B978-0-08-042066-0.50013-6 (Pergamon, 1993).
34. Drescher, K. & Handley, M. F. Aspects of time-dependent deformation in hard rock at great depth. *J. Southern African Inst. Min. Metall.* **103**(5), 325–335. https://doi.org/10.10520/AJA0038223X_2863 (2003).
35. Tran-Manh, H., Sulem, J. & Subrin, D. Progressive degradation of rock properties and time-dependent behavior of deep tunnels. *Acta Geotech.* **11**(3), 693–711. https://doi.org/10.1007/s11440-016-0444-x (2016).
36. Zhang, J. *et al.* Research on the comparison of impact resistance characteristics between energy absorption and conventional hydraulic columns in fluid–solid coupling. *Sci. Rep.* **13**(1), 20753. https://doi.org/10.1038/s41598-023-47887-y (2023).
37. Wong, L. N. Y. & Cui, X. Simulation of 3D fracture propagation under I-II-III mixed-mode loading. *Rock Mech. Bull.* **2**(4), 100082. https://doi.org/10.1016/j.rockmb.2023.100082 (2023).
38. Shang, J. Stress path constraints on veined rock deformation. *Rock Mech. Bull.* **1**(1), 100001. https://doi.org/10.1016/j.rockmb.2022.100001 (2022).
39. Gao, F., Stead, D. & Kang, H. Simulation of roof shear failure in coal mine roadways using an innovative UDEC Trigon approach. *Comput. Geotech.* **61**, 33–41. https://doi.org/10.1016/j.compgeo.2014.04.009 (2014).
40. Hosseini, N. & Khoei, A. R. Modeling fluid flow in fractured porous media with the interfacial conditions between porous medium and fracture. *Transp. Porous Media* **139**(1), 109–129. https://doi.org/10.1007/s11242-021-01648-5 (2021).
41. Reeher, L. J., Hughes, A. N., Davis, G. H., Kemeny, J. M. & Ferrill, D. A. Finding the right place in Mohr circle space: Geologic evidence and implications for applying a non-linear failure criterion to fractured rock. *J. Struct. Geol.* **166**, 104773. https://doi.org/10.1016/j.jsg.2022.104773 (2023).
42. Wang, J., Zhang, C., Zheng, D., Song, W. & Ji, X. Stability analysis of roof in goaf considering time effect. *J. Min. Strata Control Eng.* **2**(1), 013011. https://doi.org/10.16671/j.issn.2096-7187.2020.01.3011 (2020).
43. Da Fontoura, S.A.B. & Morgenstern, N.R. Stress - Strain - Time Relationship For a Jointed Coal. *ISRM International Symposium*, ISRM-IS-1981-1018. https://doi.org/10.21118/ISRMIS.1981-018 (1981).
44. Tengteng, B. Dynamic response relationship between roof movement and deformation of roadway in fully mechanized caving face of deep and thick coal seam. *J. Min. Strata Control Eng.* **3**(2), 023031. https://doi.org/10.16671/j.jmce.2021.02.023031 (2021).
45. Kang, H. Temporal scale analysis on coal mining and strata control technologies. *J. Min. Strata Control Eng.* **3**(1), 013538. https://doi.org/10.16343/j.issn.2096-6972.2021.03.013538 (2021).
46. Xu, W. *et al.* Hyper-gravity experiment of solute transport in fractured rock and evaluation method for long-term barrier performance. *Rock Mech. Bull.* **2**(3), 100042. https://doi.org/10.1016/j.rockmb.2023.100042 (2023).

47. Varkouhi, S. *et al.* Pervasive accumulations of chert in the Equatorial Pacific during the early Eocene climatic optimum. *Mar. Pet. Geol.* **167**, 106940. https://doi.org/10.1016/j.marpetgeo.2024.106940 (2024).
48. Wu, Q. *et al.* Experimental study on deformation characteristics of anchored jointed rock mass under uniaxial compression. *J. Min. Strata Control Eng.* **5**(4), 043016. https://doi.org/10.1007/s13147-022-00441-6 (2023).
49. Weijian, Y. *et al.* Experimental study on mechanical characteristics of rock of trapezoidal cross section under the equivalent non-uniform loading conditions. *J. Min. Strata Control Eng.* **6**(3), 033022. https://doi.org/10.13207/j.mse.2024.0325 (2024).
50. Li, Y., Cui, Y., Li, Y. & Gan, Y. Analysis and prediction of contact characteristics of rock fracture surfaces under normal loading. *J. Struct. Geol.* **180**, 105086. https://doi.org/10.1016/j.jsg.2024.105086 (2024).
51. Chang, X., Zhao, H. & Cheng, L. Fracture propagation and coalescence at bedding plane in layered rocks. *J. Struct. Geol.* **141**, 104213. https://doi.org/10.1016/j.jsg.2020.104213 (2020).
52. Kasyap, S. S. & Senetakis, K. Small-scale size effects on the shearing behavior and sliding stiffness reduction-displacement curves of rock-plastic gouge simulant under low normal stresses. *J. Struct. Geol.* **157**, 104553. https://doi.org/10.1016/j.jsg.2022.104553 (2022).
53. Long, Y., Chen, H., Cheng, X., Deng, H. & Lin, X. Influence of paleo-uplift on structural deformation of salt-bearing fold-and-thrust belt: Insights from physical modeling. *J. Struct. Geol.* **153**, 104445. https://doi.org/10.1016/j.jsg.2021.104445 (2021).
54. Liu, Y., Lu, C.-P., Zhang, H. & Wang, H.-Y. Numerical investigation of slip and fracture instability mechanism of coal- rock parting-coal structure (CRCS). *J. Struct. Geol.* **118**, 265–278. https://doi.org/10.1016/j.jsg.2018.11.001 (2019).
55. Adineh, S., Závada, P., Bruthans, J., Cofrade, G. & Zare, M. Growth of a salt diapir in an anticline: A record from the Cenozoic halokinetic sequences in the Zagros Fold and Thrust Belt, Iran. *J. Struct. Geol.* **178**, 105004. https://doi.org/10.1016/j.jsg.2023.105004 (2024).
56. Ma, Q., Tan, Y., Liu, X., Gu, Q. & Li, X. Effect of coal thicknesses on energy evolution characteristics of roof rock-coal-floor rock sandwich composite structure and its damage constitutive model. *Compos. B Eng.* **198**, 108086. https://doi.org/10.1016/j.compositesb.2020.108086 (2020).
57. Yu, B. *et al.* The sustainable development of coal mines by new cutting roof technology. *R. Soc. Open Sci.* **7**(6), 191913. https://doi.org/10.1098/rsos.191913 (2020).
58. Shang, Y. *et al.* Study on failure characteristics and control technology of roadway surrounding rock under repeated mining in close-distance coal seam. *Mathematics* **10**(13), 2166. https://doi.org/10.3390/math10132166 (2022).
59. Ma, X. *et al.* Lithology-controlled stress variations of Longmaxi shale: Example of an appraisal wellbore in the Changning area. *Rock Mech. Bull.* **1**(1), 100002. https://doi.org/10.1016/j.rockmb.2022.100002 (2022).
60. Zafar, S., Hedayat, A. & Moradian, O. Micromechanics of fracture propagation during multistage stress relaxation and creep in brittle rocks. *Rock Mech. Rock Eng.* **55**(12), 7611–7627. https://doi.org/10.1007/s00603-022-03045-w (2022).
61. Zafar, S., Hedayat, A. & Moradian, O. Energy budget of brittle fracturing in granite under stress relaxation and creep. *Rock Mech. Rock Eng.* **57**(2), 921–943. https://doi.org/10.1007/s00603-023-03593-9 (2024).
62. Tolouei, K., Moosavi, E., Bangian Tabrizi, A. H. & Afzal, P. Application of an improved Lagrangian relaxation approach in the constrained long-term production scheduling problem under grade uncertainty. *Eng. Optim.* **53**(5), 735–753. https://doi.org/10.1080/0305215X.2020.1746295 (2021).
63. Pincus, H.J. Rock Mechanics. in *Encyclopedia of Physical Science and Technology (Third Edition)* (ed. Meyers, R.A.) 357–379. https://doi.org/10.1016/B0-12-227410-5/00669-4 (Academic Press, 2003).
64. Wu, N., Liang, Z., Zhang, Z., Li, S. & Lang, Y. Development and verification of three-dimensional equivalent discrete fracture network modelling based on the finite element method. *Eng. Geol.* **306**, 106759. https://doi.org/10.1016/j.enggeo.2022.106759 (2022).
65. Xue, Y. Time-dependent deformation and associated failure of roof in underground mines, Ph.D. Dissertation, Graduate Theses, Dissertations, and Problem Reports. 4077., West Virginia University, 181, https://doi.org/10.33915/etd.4077 (2019).
66. Feng, X. *et al.* Orthogonal numerical analysis of deformation and failure characteristics of deep roadway in coal mines: A case study. *Minerals* **12**(2), 185 (2022).
67. Maheshwari, P. Analysis of deformation of linear viscoelastic two layered laminated rocks. *Int. J. Rock Mech. Min. Sci.* **141**, 104681. https://doi.org/10.1016/j.ijrmms.2021.104681 (2021).
68. Li, H., Zhang, H., Wu, L. & Zhou, J. Viscoelastic–plastic response of tunnels based on a novel damage creep constitutive model. *Int. J. Non-Linear Mech.* **151**, 104365. https://doi.org/10.1016/j.ijnonlinmec.2023.104365 (2023).
69. Kianoush, P., Mohammadi, G., Hosseini, S. A., Khah, N. K. F. & Afzal, P. Compressional and shear interval velocity modeling to determine formation pressures in an oilfield of SW Iran. *J. Min. Environ.* **13**(3), 851–873. https://doi.org/10.22044/jme.2022.12048.2201 (2022a).
70. Hoek, E. Strength of jointed rock masses. *Géotechnique* **33**(3), 187–223. https://doi.org/10.1680/geot.1983.33.3.187 (1983).
71. Hoek, E. & Brown, E. T. Practical estimates of rock mass strength. *Int. J. Rock Mech. Min. Sci.* **34**(8), 1165–1186. https://doi.org/10.1016/S1365-1609(97)80069-X (1997).
72. Wang, L. & Zhang, Y. Interpreting correlations in stress-dependent permeability, porosity, and compressibility of rocks: A viewpoint from finite strain theory. *Int. J. Numer. Anal. Methods Geomech.* **48**(8), 2000–2019. https://doi.org/10.1002/nag.3720 (2024).
73. Ngoma, M. C. & Kolawole, O. Assessment of nano-to-micro-scale geomechanical properties and their time-dependent behavior: Current status and progressive perspectives. *Rock Mech. Bull.* **3**(1), 100096. https://doi.org/10.1016/j.rockmb.2023.100096 (2024).

Acknowledgements

This article is based on a PhD in Mining Engineering dissertation in collaboration with the Islamic Azad University, South Tehran Branch, and the National Iranian Oil Company Exploration Directorate (NIOC-EXP). The authors would like to express their gratitude to the experts of the Reservoir Engineering and Drilling Department for their valuable assistance in providing feedback on the geomechanical model preparation.

Author contributions

A.K. Investigation, methodology, formal analysis, writing—review and editing; N.H. Formal analysis, supervision, conceptualization, investigation, methodology, laboratory tests, validation, visualization, writing—original draft, writing—review and editing; R.S. Data curation, formal analysis, laboratory tests, writing—original draft; A.H.B.T. Data curation, formal analysis, laboratory tests, writing—original draft; M.G. Data curation, formal analysis, laboratory tests, writing—original draft; P.K. Conceptualization, investigation, methodology, laboratory tests, visualization, writing—original draft, writing—review and editing.

Funding

This research did not receive any specific grant from funding agencies in the public, commercial, or not-for-profit sectors.

Competing interests
The authors declare no competing interests.

Additional information
Supplementary Information The online version contains supplementary material available at https://doi.org/10.1038/s41598-024-69854-x.

Correspondence and requests for materials should be addressed to N.H.

Reprints and permissions information is available at www.nature.com/reprints.

Publisher's note Springer Nature remains neutral with regard to jurisdictional claims in published maps and institutional affiliations.